PSR Report 2436

PRACTICAL PERFORMANCE MODEL FOR AIRBORNE LIDAR IN UNDERSEA WARFARE

P. M. Moser

February 1994
Revised August 1994

Phase Report
Contract N62269-90-C-0551

REPORT DOCUMENTATION PAGE

1. REPORT DATE (DD-MM-YYYY)	2. REPORT TYPE	3. DATES COVERED (From - To)
xx-08-1994	Phase technical	To August 1994

4. TITLE AND SUBTITLE	5a. CONTRACT NUMBER
Practical Performance Model for Airborne Lidar in Undersea Warfare	N62269-90-C-0551
	5b. GRANT NUMBER
	5c. PROGRAM ELEMENT NUMBER
6. AUTHOR(S)	5d. PROJECT NUMBER
Moser, Paul M.	
	5e. TASK NUMBER
	5f. WORK UNIT NUMBER

7. PERFORMING ORGANIZATION NAME(S) AND ADDRESS(ES)	8. PERFORMING ORGANIZATION REPORT NUMBER
Pacific-Sierra Research Corporation Warminster, PA 18974	PSR Report 2436

9. SPONSORING/MONITORING AGENCY NAME(S) AND ADDRESS(ES)	10. SPONSOR/MONITOR'S ACRONYM(S)
Naval Air Warfare Center Aircraft Division Warminster	NAWCADWAR
	11. SPONSOR/MONITOR'S REPORT NUMBER(S)

12. DISTRIBUTION/AVAILABILITY STATEMENT
Approved for public release, distribution unlimited

13. SUPPLEMENTARY NOTES

14. ABSTRACT
This report describes a mathematical model for making first-order assessments of the potential performance of airborne lidar in undersea warfare with a minimum of generally available input values. The model is based on the ORADS "range equations" of 1976 which have been extended to address area search by a scanning lidar and the integrated effect of multiple "hits" on the target. It permits one to interrelate operational, environmental, sensor, and target parameters in ways that enable calculation of tactical performance parameters such as search rate vs. water clarity and target depth, sensor operating altitude and field of view, and target detection depth for submarines and mines in day and nighttime operations.

15. SUBJECT TERMS
Lidar, Laser, Aircraft, Undersea Warfare, Nonacoustic Detection, Submarine, Mine,

16. SECURITY CLASSIFICATION OF:			17. LIMITATION OF ABSTRACT	18. NUMBER OF PAGES	19a. NAME OF RESPONSIBLE PERSON
a. REPORT	b. ABSTRACT	c. THIS PAGE			
unclassified	unclassified	unclassified	unlimited	80	19b. TELEPHONE NUMBER (Include area code)

Standard Form 298 (Rev. 8/98)

CONTENTS

CONTENTS (continued)

iv

FIGURES

FIGURES (continued)

TABLES

ABSTRACT

A mathematical performance model has been developed to provide inputs to required operational effectiveness assessments and Cost-Effectiveness Analyses (COEA) of airborne undersea warfare (USW) lidar. Lidar is a candidate for development under the Advanced Technology Demonstration (ATD) program. The model is essentially the ORADS "range equations" of 1976 which have been extended to address the topics of area search by a scanning lidar and the integrated effect of multiple "hits" on target whereas the original ORADS equations covered only "single-hit" detection. The model permits one to interrelate operational, environmental, sensor, and target parameters in ways that enable calculation of tactical performance parameters such as search rate vs. water clarity and target depth, optimum operating altitudes and sensor fields of view, and detection depth capability. The model is applicable to both submarine and moored mine detection in day and nighttime operations.

The model is referred to as "practical" because it is designed to provide first-order answers relevant to operational effectiveness assessments with a minimum of generally available input values. The target is assumed to be a right circular cylinder whose longitudinal axis is horizontal and which can take on any orientation relative to the plane of incidence of the laser beam. The effective area of the target and the duration of the return pulses are expressed as functions of target orientation and angle of incidence at the sea surface. The model assumes that the lidar transmitted and received pulses are rectangular in shape and that they can be characterized in terms of peak power and pulse duration. No attempt is made, for example, to calculate the detailed shape of the return pulse taking into account multiple scattering in seawater and reflection of the extended pulse off the complex surface of a real target. It is believed, however, that the model is sufficiently rigorous for its intended purpose.

INTRODUCTION

The Navy is developing technology for new and improved nonacoustic air undersea warfare sensor subsystems such as periscope detection radar, magnetic anomaly detector (MAD), and lidar. Sensors in these three categories are either currently under development or are candidates for development under the Advanced Technology Demonstration (ATD) program.

Crucial to the development of these ATDs are supporting operational effectiveness assessments. These assessments serve as inputs to Cost-Effectiveness Analyses (COEA) which are required by RDT&E authorities to make informed decisions regarding potential transitions to Engineering Manufacturing Development (6.4).

A study was begun in July 1993 to determine, for PEO(A)/PMA-264, the performance capability and the operational utility of several assumed levels of technological maturity of airborne lidar, radar and MAD for USW applications. The focus is on the detection/localization of submarines and mines, by use of helicopters and fixed wing aircraft, in a potential shallow water/regional conflict, small-area search scenario in selected Defense Planning Guidance (DPG) regions such as the Persian Gulf, the Strait of Hormuz, and the Gulf of Oman.

The present report focuses on airborne USW lidar. The planned procedure was to select or develop an appropriate performance model that would enable calculating area search rate as a function of target depth for submarines and mines in a selected DPG geographic location/scenario for several different levels of water clarity for the following assumed levels of lidar technology: "baseline" for helicopters, "enhanced" for helicopters, "baseline" for fixed wing aircraft, and "enhanced" for fixed wing aircraft. The outputs of the sensor performance model would then serve as inputs to tactical utility models such as the NAWCADWAR DIASS (Detection by Integrated ASW Sensor Suites) multisensor engagement model to assess the utility of the sensor alone and to determine the incremental gain provided by the sensor as part of an acoustic/nonacoustic sensor suite.

None of the previously existing available models were capable of providing the desired outputs. Accordingly, the ORADS range equations, which are given in reference (a), were extended to meet the needs and programmed for use on an IBM-compatible personal computer. This report documents the model that evolved and illustrates its use as a tool when applied to a number of hypothetical situations. The examples presented do not represent any current or future planned equipments.

DISCUSSION

Four classes of parameters govern the performance of any sensor: (1) target characteristics, (2) sensor characteristics, (3) environmental parameters, and (4) operational parameters. In this study, the performance of lidar is defined in terms of its design characteristics subject to the constraints imposed by the environment, the target, and the operational situation.

Airborne lidars have the potential for detecting and precisely localizing underwater targets such as submarines and mines. However, there is currently a severe lack of performance and operational utility data for lidars in these roles. Although air-to-underwater "technical" models exist which address the reflection of single pulses of light from an underwater target, there were no practical models available which could be readily used to characterize the potential tactical performance of an airborne lidar in various regional conflict/littoral warfare scenarios.

A practical lidar performance model, based on the ORADS range equations, has been developed and exercised; its principal output is the interdependent area search rate of any specified lidar as a function of target type and geographical location. The lidar performance model accepts (directly or indirectly) sensor parameters such as laser average power, transmitted pulse length, beam divergence, scanner lateral field of view, effective area of the receiver optics, transmittance of the receiver optics, optical filter spectral transmittance, and detector quantum efficiency; environmental parameters such as seawater attenuation coefficient, bulk upwelling of backscattered sunlight, altitude of the cloud base, and atmospheric visibility range; target characteristics such as length, diameter, and reflectivity; and operational parameters such as target depth and aircraft altitude and speed.

The foregoing parameters are all interrelated. For example, because a cloud-free line of sight is required between the sensor and the sea surface, the aircraft must operate below the cloud base, if any. Therefore, it is necessary to consider cloud statistics for the operating areas and seasons of interest and to design the lidar and exercise it at altitudes for which successful operation is possible. Similarly, spectral water clarity, which is the principal environmental determiner of USW lidar performance, varies considerably with geographical location and season and is a key driver in choosing laser parameters such as wavelength and average power.

The output of the lidar practical performance model will serve as an input to tactical utility models such as the DIASS engagement model. DIASS will be exercised with other airborne USW sensor systems, with and without lidar, to determine the incremental improvement in utility that accrues from the use of lidar, and the expected payoff in

3

enhanced system capability. The DIASS output will be in terms of *probability of detection opportunity* which will serve as a measure of effectiveness/utility of the system in the various USW scenarios. Results of the DIASS analyses will be fed back into the lidar performance model to arrive at optimum sets of sensor parameters for the various scenarios. For example, in certain situations, only moderate detection depth capability may be required; this would allow trading-off this parameter for increased area search rate.

THE BASIC LIDAR MODEL - ORADS (1976)

Reference (a) provides equations interrelating most of the key USW lidar parameters. These equations are, for the nighttime and daytime cases, respectively,

Nighttime

$$\exp\left[KD\left(1-9/16\sin^2\theta\right)^{-1/2}\right](D+H)\left(1-9/16\sin^2\theta\right)^{-1/2}$$

$$= \frac{\left\{P_xS(t_x/t_r)^2\,A_R\,T_R\,T_{AW}^2\,T_A^2\,(\rho_T F)^2\right\}^{1/2}}{\left\{2\,\pi\,(SNR)\,e\,\Delta f\,\rho_w\right\}^{1/2}} \qquad (1)$$

Daytime

$$\exp\left[KD\left(1-9/16\sin^2\theta\right)^{-1/2}\right](D+H)\left(1-9/16\sin^2\theta\right)^{-1/2}$$

$$= \frac{\left\{P_xS(t_x/t_r)\,A_R\,T_R\,T_{AW}^2\,T_A^2\,H\,(\rho_T F)\sec\theta\right\}^{1/2}}{\left\{\pi\left[\pi/2\,(SNR)\,e\,\Delta f\,S\,T_R\,N_\lambda\,A_R\,\Delta\lambda\right]^{1/2}\,d_s\right\}^{1/2}} \qquad (2)$$

Definitions of the terms used in these equations are included in the following list of symbols.

Symbol	Definition	Unit
A_R	area of receiver aperture	m^2
A_T	area of target	m^2
D	depth; depth of target	m
d_s	diameter of laser spot incident on water surface	m
e	electronic charge (1.602×10^{-19})	C
F	geometrical form factor (ratio of beam power incident on target to total beam power in horizontal plane of target)	

Symbol	Definition	Unit
Δf	frequency bandwidth	Hz
H	aircraft altitude (laser transceiver altitude)	m, ft
K	diffuse attenuation coefficient of water	m^{-1}
N_λ	upwelling background spectral radiance	$W \cdot m^{-2} \cdot sr^{-1} \cdot nm^{-1}$
P_x	peak power transmitted	W
S	photocathode radiant sensitivity	A/W
SNR	ratio of signal power to noise power	
T_A	transmittance of atmospheric path	
T_{AW}	transmittance of air/water interface	
T_R	transmittance of receiver optics	
T_W	transmittance of path through water	
t_r	duration of received pulse	ns
t_x	duration of transmitted pulse	ns
λ	wavelength	nm
$\Delta\lambda$	optical bandwidth of predetection filter	nm
ρ_T	reflectivity of target	
ρ_W	reflectance of slab of water	
θ	transmitter/receiver scan angle measured from vertical; angle of incidence	deg

LIMITATIONS OF THE BASIC ORADS EQUATIONS

The basic ORADS equations suffer certain limitations which are addressed in this model. Equations (1) and (2) were developed for the case of a single pulse of initial peak power P_x impinging on the center of the target. The ORADS equations do not address issues associated with area search such as aircraft speed, scanner lateral field of view, pulse repetition rate, and multiple hits on the target. The ORADS equations assume that the target behaves as a flat plate of uniform reflectivity normal to the incident laser beam.

The ORADS equations tacitly include the assumption that rays of light reflected from the target diverge at an angle that is constant from the target to the sensor. On the contrary, upon refraction at the surface, the solid angle containing a bundle of rays increases, resulting in a reduced power density at the receiver relative to what a simple inverse square law dependence would imply.

MODIFICATIONS TO THE BASIC ORADS EQUATIONS

The following treatment expands the basic ORADS equations to cover the issues of target orientation, area search rate and the improvement in detectability resulting from multiple hits on the target.

Figure 1 illustrates the geometry of a scanning lidar and some of the terms used in the following equations. L is the length of the in-water path taken by the laser pulse to the target at depth D. Then, in equations (1) and (2), the factor $(1 - 9/16 \sin^2 \theta)^{-1/2}$ can be written more generally and compactly as

$$(1 - n^{-2} \sin^2 \theta)^{-1/2} = L/D = G \qquad (3)$$

in which n is the index of refraction of seawater with respect to air.
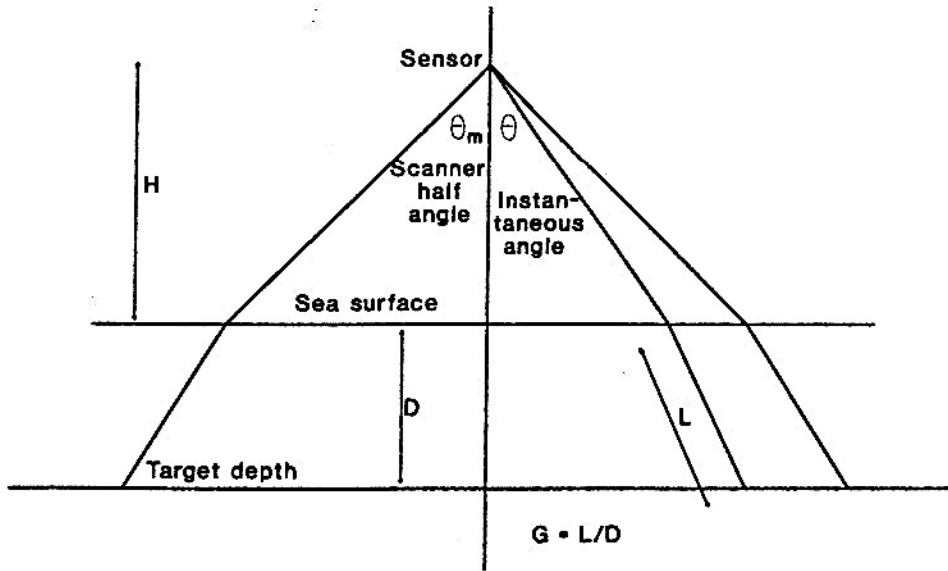
Figure 1. Lidar lateral scan geometry.

It is assumed that the laser output can be represented as a sequence of well-defined rectangular pulses as shown in figure 2. If the lidar pulse repetition period is t_p, then the average power

$$P_{av} = P_x t_x/t_p = P_x t_x (PRF) \qquad (4)$$

in which PRF is the pulse repetition rate.
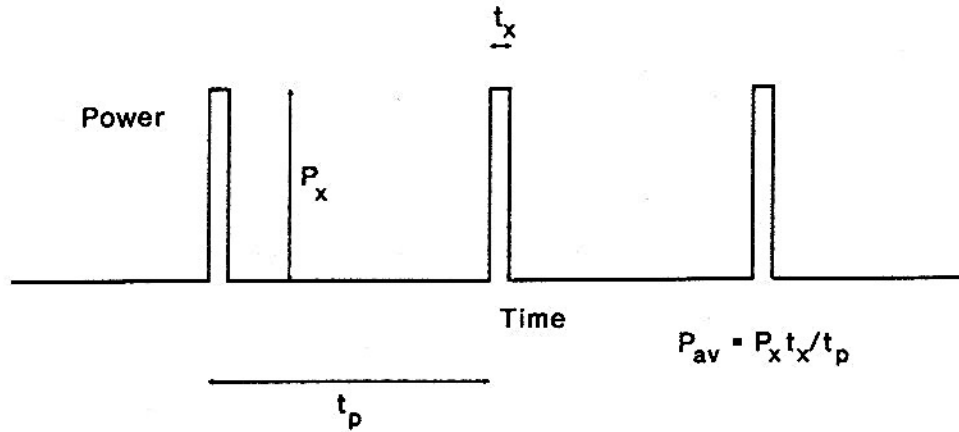
Figure 2. Laser power output as a function of time.

To interrelate laser PRF, aircraft speed and altitude, and lidar spatial resolution, three approaches which can be used in the model are considered: (1) scanning spots of constant area on the sea surface, (2) laser beam of constant solid divergence angle, and (3) laser beam whose diameter is constant at the sea surface. In the case of a circular (conical) scanner, all three of these conditions can coexist simultaneously. On the other hand, to satisfy situation (1) or (3) with a line scanner, it is necessary to control the beam divergence as a function of angle of incidence of the laser beam at the sea surface.

In the following, it is assumed that the region of space under observation will be populated by laser spots with a fill factor f. If the space is completely filled, with neither overlaps or underlaps, f = 1.

The case that is simplest conceptually, but perhaps most difficult to implement (except for a circular scanner) is the one in which the area, shape, and orientation of the scanning spot on the surface remain constant throughout the scan cycle. Figure 3 illustrates the situation for a special type of line scanner in which the beam divergence and cross-section are adjusted continuously as a function of scan angle to yield a square spot on the surface. In practice, for such a situation, it is necessary to adjust, during each scan, the rectangular cross-section of the laser beam and, for constant PRF, the scan angular velocity.

Let ΔA represent the area of the laser spot at the surface of the water, v equal the speed of the aircraft carrying the lidar, θ_m equal the lidar lateral scan half angle, and e_{sc} equal the scan efficiency. As shown in figure 3, in time t, the scanner will sweep out a swath of area

$$A_s = 2 \, v \, t \, H \tan \theta_m. \tag{5}$$

9
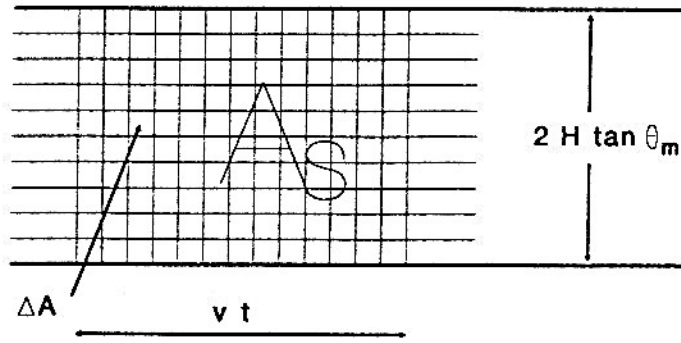
Figure 3. Surface search area covered by a scanning lidar
for fill factor f = 1.

For scanning that is contiguous at the sea surface, the required PRF of the lidar is
given by

$$PRF = (2 f v t H \tan \theta_m)/(\Delta A\ t\ e_{sc}) = (2 f v H \tan \theta_m)/(\Delta A\ e_{sc}). \qquad (6)$$

The second approach to laser beam management for a line scanner is to maintain a
beam of constant solid divergence angle. The relative angular velocity of the scene directly
below the aircraft is v/H (rad/s). If the lateral half-angle field of view is θ_m (rad), then the
scanner sweeps out solid angle at the rate of $2 v \theta_m/H$ (sr/s). If the laser beam has a
rectangular cross-section and subtends an angle α (rad) in the lateral direction and β (rad) in
the fore/aft direction, then the pulse repetition rate PRF_{ang} required for the beams to be
contiguous in solid angle is

$$PRF_{ang} = 2 v \theta_m f / (\alpha \beta H e_{sc}). \qquad (7)$$

The scan rate v required for contiguous angular scanning directly below the aircraft is

$$v = v / (H \beta). \qquad (8)$$

In certain situations it may be appropriate to maintain a constant beam diameter (at
the sea surface) or even to reduce the beam diameter as the angle of incidence increases. An
objective of the latter situation would be achievement of a detection depth capability that is
independent of angle of incidence. This could require some combination of varying scan
angular velocity and PRF as a function of scan angle. Because the optimum manner in
which these parameters would vary is a function of factors such as water clarity and target
depth, this method is not addressed here in a general way.

10

For the first of these approaches the fill factor is assumed to be unity and equations (4) and (6) are combined to yield

$$P_x = (P_{av} \, \Delta A \, e_{sc})/(2 \, v \, H \tan \theta_m \, t_x). \tag{9}$$

Let the receiver frequency bandwidth

$$\Delta f = 1/t_r . \tag{10}$$

Let T_F equal the in-band transmittance of the optical filter (if any). That is, in equation (1), replace T_R by the product $T_R \cdot T_F$.

Substitution of equations (3), (9) and (10) into equation (1) and squaring both sides of the resulting equation yields

$$\exp[2 \, KDG] \, (D+H)^2 \, G^2 = \frac{P_{av} \, \Delta A \, e_{sc} \, S \, (t_x/t_r) \, A_R \, T_R \, T_F \, (T_A \, T_{AW} \, \rho_T)^2 \, F^2}{4 \, \pi \, v \, H \tan \theta_m \, (SNR) \, e \, \rho_w} \tag{11}$$

Equation (11) includes a square law spreading factor $(D+H)^2$, which does not take into account the increased spreading that occurs because of refraction of light reflected from the target as it emerges from the water into the air. In this model, the factor $(D+H)^2$ is replaced by the factor BH^2 in which B is the ratio of the solid angle angle subtended by a bundle of rays in air at the water surface to the smaller solid angle subtended at the target by the same bundle of rays.

For a target presenting an area A_T at or very near to the water surface, the number of laser hits on the target will be $A_T/\Delta A$. However, because of spreading of the laser beam as it passes through the water, spots that were contiguous at the surface will be overlapping at depth. If A_{sp} is the cross-sectional area of the laser beam at the location of a submerged target, the number of hits on the submerged target will increase by a factor of $(A_{sp}/\Delta A)^{1/2}$. Thus the number of hits N on a target will be

$$N = (A_T/\Delta A)(A_{sp}/\Delta A)^{1/2}. \tag{12}$$

The power signal-to-noise ratio (SNR) which appears in equations (1) and (2) is that required to achieve a given probability of detection (P_D) and a given false alarm rate (P_{FA}) on the basis of a single hit on the target. Reference (a) suggests a value of SNR = 17 for $P_D = 0.95$ and $P_{FA} = 10^{-4}$. The power signal-to-noise ratio required to achieve the same values of P_D and P_{FA} when N hits occur on target would be 1/N times as great. Accordingly,

for a system capable of perfectly integrating signals from multiple hits, the following substitution should be made

$$(SNR) \rightarrow (SNR)/N = (SNR)(\Delta A/A_T)(\Delta A/A_{sp})^{1/2}. \qquad (13)$$

If equation (13) is inserted into equation (11), the substitution $(D + H)^2 \rightarrow BH^2$ carried out, and the factors rearranged in the resulting equation to place sensor parameters on the right side of the equation and operational, environmental, and target parameters on the left side, the following is obtained for the nighttime situation.

$$\frac{B\,H^2\,G^2\,(SNR)\,(\Delta A)^{1/2}\,(v\,H\,\tan\theta_m)\,(4\,\pi\,e\,\rho_w\,t_r/t_x)\,\exp[2\,KDG]}{F^2 \quad A_T\,(A_{sp})^{1/2} \quad (T_A\,T_{AW}\,\rho_T)^2}$$

$$= P_{av}\,e_{sc}\,S\,A_R\,T_R\,T_F \qquad (14)$$

Similarly, if equations (3), (9), (10), and (13) are substituted into equation (2) and BH^2 substituted for $(D + H)^2$, the following expression is obtained for the daytime situation.

$$\frac{B\,H^2\,G^2\,(SNR)^{1/2}\,(\Delta A)^{1/4}\,(v\,\tan\theta_m)\,(2\,\pi\,\cos\theta)\,(2\,e\,N_\lambda\,t_r)^{1/2}\,\exp[2\,KDG]}{F \quad A_T^{1/2}\,A_{sp}^{1/4} \quad (T_A\,T_{AW})^2\,\rho_T}$$

$$= P_{av}\,e_{sc}\,[S\,A_R\,T_R\,T_F/(\Delta\lambda)]^{1/2} \qquad (15)$$

12

ELUCIDATION OF TERMS USED IN
LIDAR PERFORMANCE MODEL EQUATIONS

Before one can use equations (14) and (15), it is necessary to describe the quantities used in terms of other more readily determinable quantities.

Photocathode Radiant Sensitivity

The photocathode radiant sensitivity S can be related to quantum efficiency in the following manner:

$$S = (e\lambda/hc)\,(Q.E.) = \lambda\,(Q.E.)/1239.8 \tag{16}$$

in which

λ is the lidar wavelength in nm
h is Planck's constant
c is the speed of light in free space, and
Q.E. is the quantum efficiency of the detector.

Since Q.E. $\leq$ 1, for a wavelength of 532 nm, S cannot exceed the value 0.429 A/W.

Scan Efficiency

The scan efficiency e_{sc} is a measure of how well the lidar scans out the scene under surveillance relative to an ideal lidar. An example of an ideal lidar is one which illuminates the water surface with no gaps in space or time and no overlaps. A line scanner, for example, that produces contiguous spots on the surface but which requires a 10% dead time between successive scans would have a scan efficiency of 90%. A circular (conical) scanner used in an aircraft in which forward motion of the platform provides forward coverage spends a disproportionately large portion of the time at the left and right edges of the scene; consequently, there is considerable scan overlap at the edges of gaps near the center. Even though there is no dead time in a circular scanner, the ratio of the number of laser shots required per complete scan cycle to sweep out a swath of width 2r relative to a line scanner is $2\pi r/2r = \pi$; the corresponding scan efficiency is $1/\pi = 0.318$. If both the forward and aft portions of the circular scan are used in an integrated fashion, the scan efficiency is $2/\pi = 0.637$.

Transmittance of Light Through the Atmosphere

In this model it is assumed that the attenuation coefficient of the atmosphere is independent of altitude and direction. For the wavelength interval 380 to 720 nm, the transmittance T_A of a slant atmospheric path from altitude H to the surface can be expressed in terms of the "visibility" or "meteorological range" R_V by

$$T_A = \exp [(-0.003912\ H)/(R_V \cos \theta)] \qquad (17)$$

in which R_V is expressed in km (but H is in m). Equation (17) was adapted from reference (b).

Figure 4 is a plot of equation (17) showing the one-way transmittance through the atmosphere to the ocean surface from a sensor altitude of 1000 m as a function of viewing angle relative to the vertical for four values of atmospheric visibility. Typical transmittances are of the order of 0.5 to 0.8.
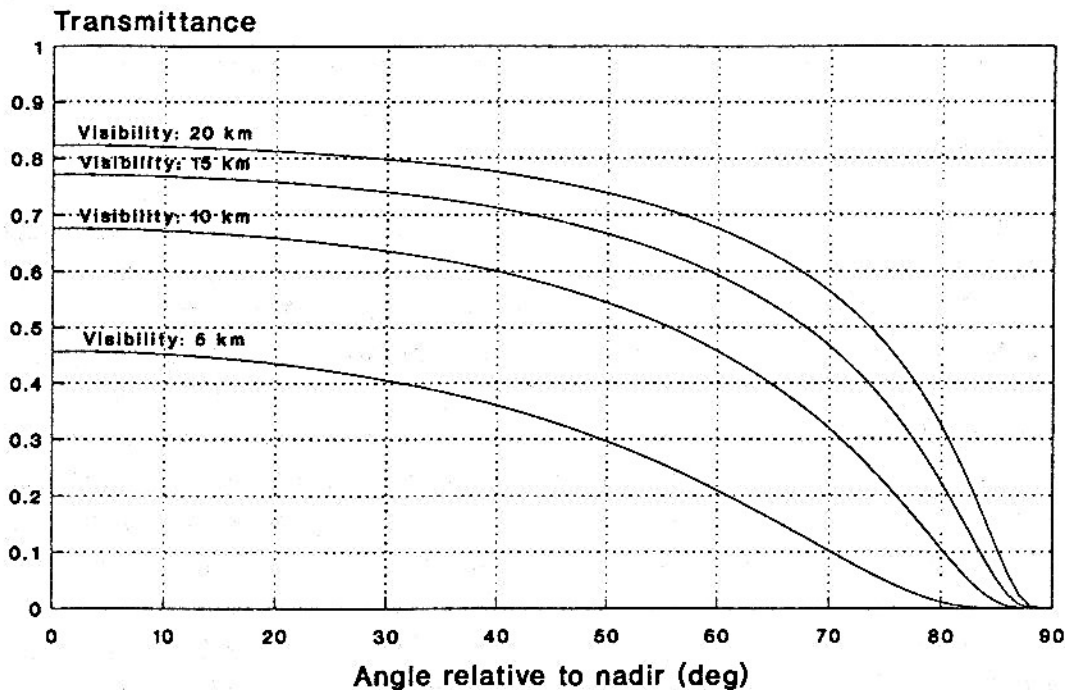
Transmittance

Figure 4.   One-way transmittance over an atmospheric path to the surface from an altitude of 1000 m as a function of angle relative to the nadir.

Wavelength range: 380 to 720 nm. A "flat earth" was assumed.

14

Transmittance of Light Through the Air-Water Interface

The transmittance T_{AW} of unpolarized light through a smooth air-water interface as a function of angle of incidence θ is obtained from Fresnel's laws of reflection at a dielectric surface.

$$T_{AW} = 1 - \sin^2(\theta-\theta')/[2 \sin^2(\theta+\theta')] - \tan^2(\theta-\theta')/[2 \tan^2(\theta+\theta')] \qquad (18)$$

in which the angle of refraction θ' is given by

$$\theta' = \arcsin [(\sin \theta)/n].$$

Figure 5 is a plot of equation (18) which shows how the transmittance of an air-water interface varies as a function of angle of incidence. As the angle relative to the nadir increases, the fraction of the light that is reflected increases and the amount that is transmitted decreases accordingly. At normal incidence, about 98% of the incident power is transmitted; at an incidence angle of 60°, about 94% is transmitted. For larger angles, the dropoff rate becomes much more severe.
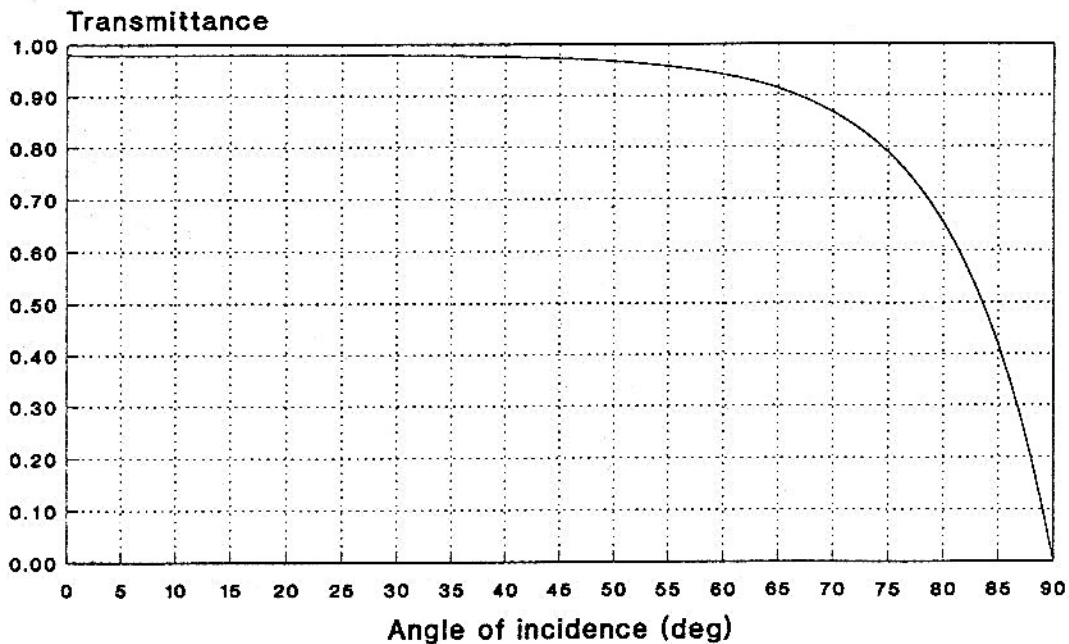
Figure 5. Transmittance of unpolarized light through a smooth air-water interface as a function of angle of incidence.

Transmittance of Light Through Seawater

For USW lidar purposes, the transmittance of light through sea water is often expressed in terms of the diffuse attenuation coefficient K, which is a function of the water type and the wavelength of light. K is the reciprocal of attenuation length, which, in turn, is the path length through water over which the power density of a beam of light is reduced to $1/e$ (36.8%) of its initial value. K is expressed in reciprocal meters or m^{-1}.

Jerlov (reference (c)) has defined ten types of waters: five ocean types (I, IA, IB, II and III) and five coastal types (1, 3, 5, 7, and 9). Jerlov's values of K are plotted as functions of wavelength in figure 6. The clearest ocean water (Ocean I) exhibits a minimum attenuation coefficient of about 0.02/m at a wavelength of 475 nm in the blue region of the spectrum. At 532 nm, the wavelength of green light from the commonly used frequency-doubled Nd:YAG (neodymium-doped yttrium aluminum garnet) laser, K = 0.05/m in the clearest waters. As one goes to more turbid waters, the minimum of the curve broadens and shifts to the longer wavelengths. For Jerlov ocean type III water, K is essentially constant over the wavelength range of 475 to 550 nm with a value of about 0.12/m .
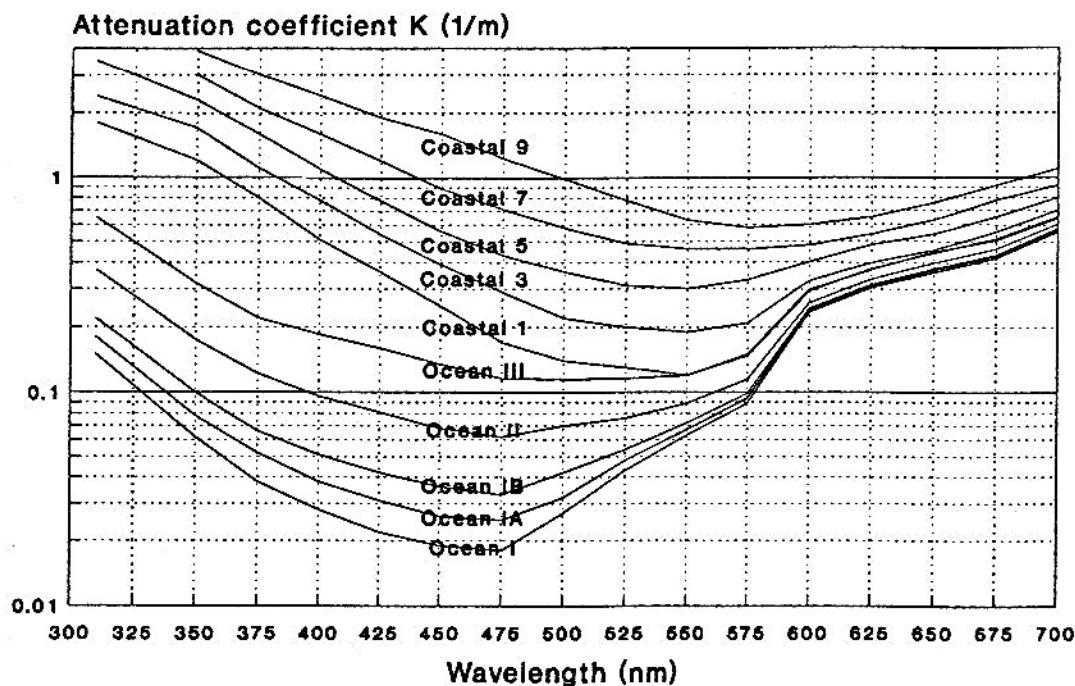
Figure 6. Diffuse attenuation coefficient as a function of wavelength for ten types of seawater.

Data were taken from table XXVII of reference (c).

16

The exponential factor in equations (1) and (2) represents the reciprocal of the one-way transmittance of light through through sea water. In figure 7, this reciprocal is plotted for five values of K. If figure 7 is compared to figure 4, it is seen that for even very clear ocean water (K = 0.03/m), the transmittance over a path length as small as 25 m is about equivalent to the transmittance over an atmospheric path of 1000 m under hazy conditions (visibility = 5 km). Stated differently, such very clear ocean water would exhibit a "visibility" of only about 0.13 km.
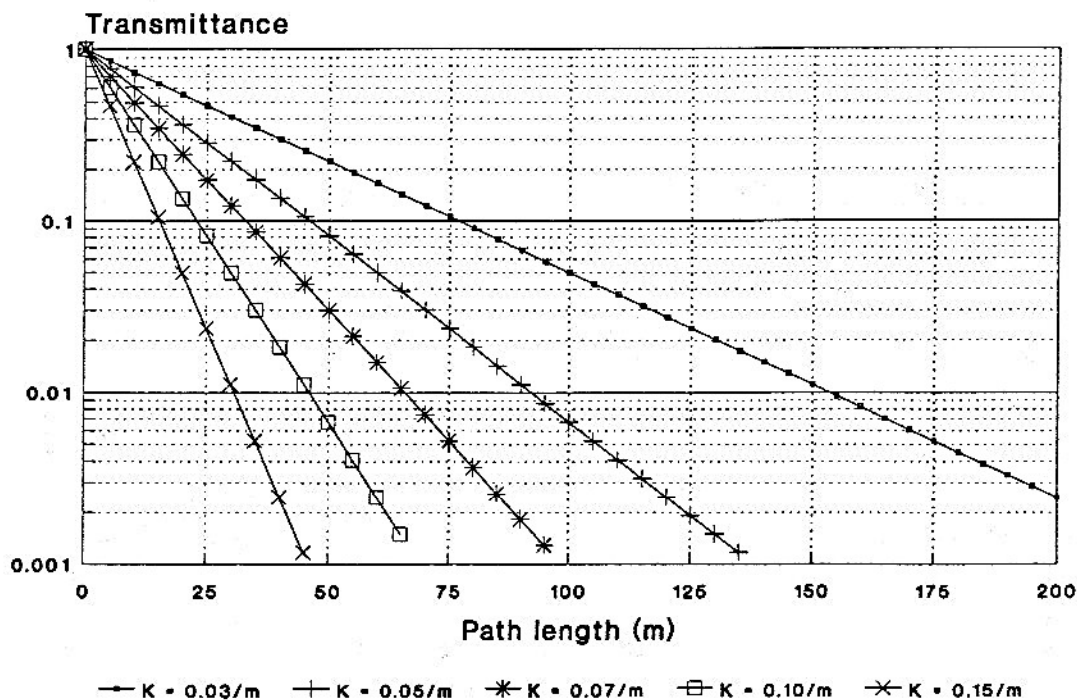
Figure 7. One-way transmittance of light through seawater for five values of diffuse attenuation coefficient K.

Upwelling Background Spectral Radiance

In daytime operations, a USW lidar must contend with the upwelling of solar radiation from the surface, the body of the water, and the ocean bottom. In regions of shallow but clear water, a significant portion of this radiation may be sunlight reflected from the sea floor. In regions where there is a large silt burden, such as outfalls of large rivers, reflection of sunlight from mineral particles may dominate the upwelling. However, for most regions of USW interest, the principal cause of solar backscatter is chlorophyll, a constituent of marine plants. Thus upwelling background radiance exhibits geographical and seasonal variations as well as diurnal variations related to sun elevation angle.

17

Figure 8 illustrates the spectral flux density of upwelling solar radiation as a function of wavelength for three values of chlorophyll concentration. Figure 8 was prepared by combining somewhat inconsistent data provided in figure 3-123 and table 3-18 of reference (d). It should be noted that figure 8 gives values of spectral flux density in units of $W \cdot m^{-2} \cdot nm^{-1}$ whereas equations (2) and (15) require units of $W \cdot m^{-2} \cdot sr^{-1} \cdot nm^{-1}$. If one makes the assumption that chlorophyll in water behaves as a diffuse Lambertian reflector, one can make the conversion to the units of equations (2) and (15), for the case of viewing normal to the surface, by dividing by π. Reference (a) gives a single measured value of $0.02 \ W \cdot m^{-2} \cdot sr^{-1} \cdot nm^{-1}$ for a sun elevation angle of about 40° on a fairly clear day.
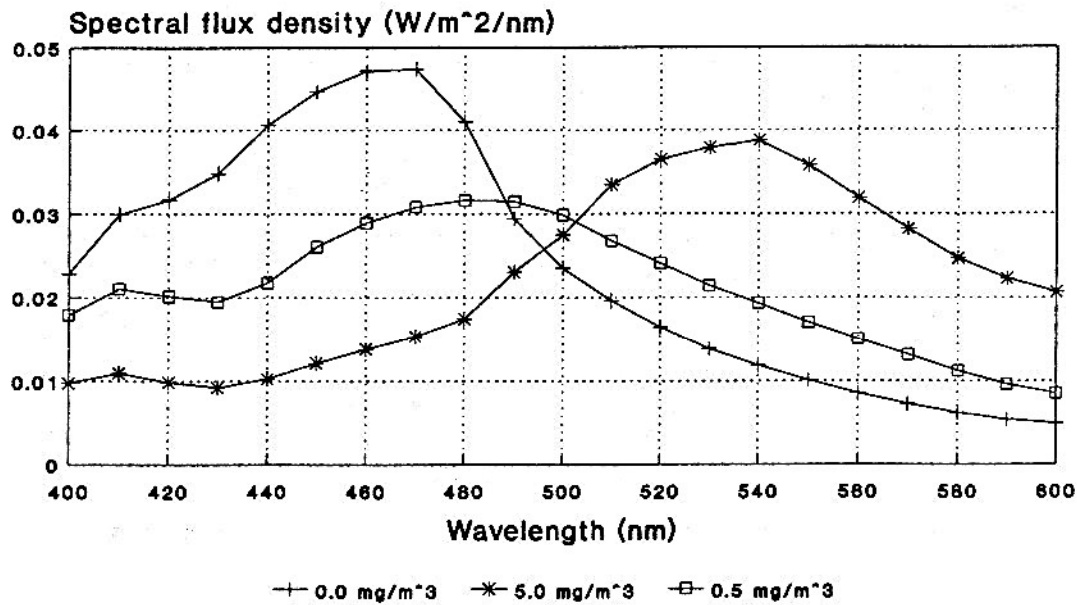
Figure 8.   Spectral upwelling of solar radiation from deep ocean water for various concentrations of chlorophyll.

Values include surface reflection from a smooth ocean. Solar zenith angle 45° to 60°.

Cross-Sectional Area of Laser Beam at Target Location

In this model, four factors are considered which contribute to the cross-sectional area A_{sp} of the laser beam at the location of a submerged target: (1) the initial beam divergence half angle φ of the laser and the path length to the water surface, (2) the reduction in the

beam divergence angle because of refraction upon incidence of the beam on a smooth water surface, (3) the increase in beam divergence angle because of water surface roughness, and (4) the spreading of the beam because of multiple scattering as the light passes through the body of the water. In the following, the curvature of the earth is ignored; i.e., the earth is assumed to be flat.

(1) Reduction of beam divergence angle upon refraction

The initial beam divergence half angle φ of the laser in terms of the diameter D_I of the laser beam (perpendicular to the direction of propagation) at the surface of the water is given by

$$\varphi = \arctan (D_I \cos \theta / (2 H). \tag{19}$$

After refraction, the extreme rays of the beam will propagate at angles σ and μ relative to the normal to the surface.

$$\sigma = \arcsin\{[\sin(\theta+\varphi)]/n\} \tag{20}$$

$$\mu = \arcsin\{[\sin(\theta-\varphi)]/n\} \tag{21}$$

The diameter D_R of the cross section of the beam at the target location from the initial divergence of the beam and refraction at the water surface is

$$D_R = D_I + GD \tan(\sigma-\theta') + GD \tan(\theta'-\mu). \tag{22}$$

(2) Increase of beam divergence angle from surface waves

Reference (a) provides a theoretical curve for the contribution to the beam divergence half angle at the air-water interface because of wind-driven waves at the surface. The equation

$$\varphi_W = 1.66 \, v_W^{0.5} \tag{23}$$

provides a good representation of the curve. In equation (23), φ_W is the total half-power beam divergence in degrees and v_W is the wind speed in m/s.

The contribution D_W to the diameter of the cross section of the beam at the target location from wind-driven surface waves is

$$D_W = 2 \, G \, D \tan(\varphi_W/2) = 2 \, G \, D \tan(0.83 \, v_W^{0.5}). \tag{24}$$

19

(3) Increase of beam divergence from scattering

There is currently a dearth of validated measurements of the spreading of the laser beam as the light passes through a body of seawater and experiences multiple scattering by suspended particulates. Fujimura has analyzed LIDEX data (reference (e)) which included measurements over water path lengths up to two attenuation lengths. (It would be desirable to cover up to about six attenuation lengths.) Fujimura has developed a simple empirical equation based on those data which enables one to calculate the diameter D_S of the cross section of the beam that contains 50% of the radiant power at the location of the target:

$$D_S = 2 \, G \, D \, \tan(1.16 \, (K \, G \, D)^{1.57}) \tag{25}$$

in which the argument of "tan" is considered to be in degrees.

(4) Combined effect of beam divergence mechanisms

The diameter D_{sp} of the beam cross section containing 50% of the power at depth D may be obtained by taking the square root of the sum of the squares of each of the contributing factors from equations (22), (24), and (25). That is,

$$D_{sp}^2 = D_R^2 + D_W^2 + D_S^2 \tag{26}$$

and the corresponding cross-sectional area A_{sp} is

$$A_{sp} = (\pi/4) \, D_{sp}^2. \tag{27}$$

Projected Length of a Horizontal Target

In this model the target is assumed to be a right circular cylinder whose longitudinal axis is horizontal. This axis can be oriented at any angle Γ from 0° to 90° relative to the plane of incidence of light from the lidar. Thus $\Gamma = 90°$ if the target is viewed from the beam aspect and 0° if it is viewed from the bow or stern aspect. The projected length l_p of the target, which is contained implicitly in equations (14) and (15) in the area of the target A_T, and in the geometrical form factor F, is a function of both Γ and of θ or θ', as expressed in the following equation:

$$l_p = l \cos(\theta' \cos \Gamma) = l \cos \{\arcsin [(\sin \theta)/n] \cos \Gamma \}. \tag{28}$$

Figure 9 is a plot of l_p as a function of θ for five values of target orientation. Note that, as should be expected, for an incidence angle of 0°, the projected target length is

20

independent or target orientation and, from the beam aspect, the projected length is independent of angle of incidence.
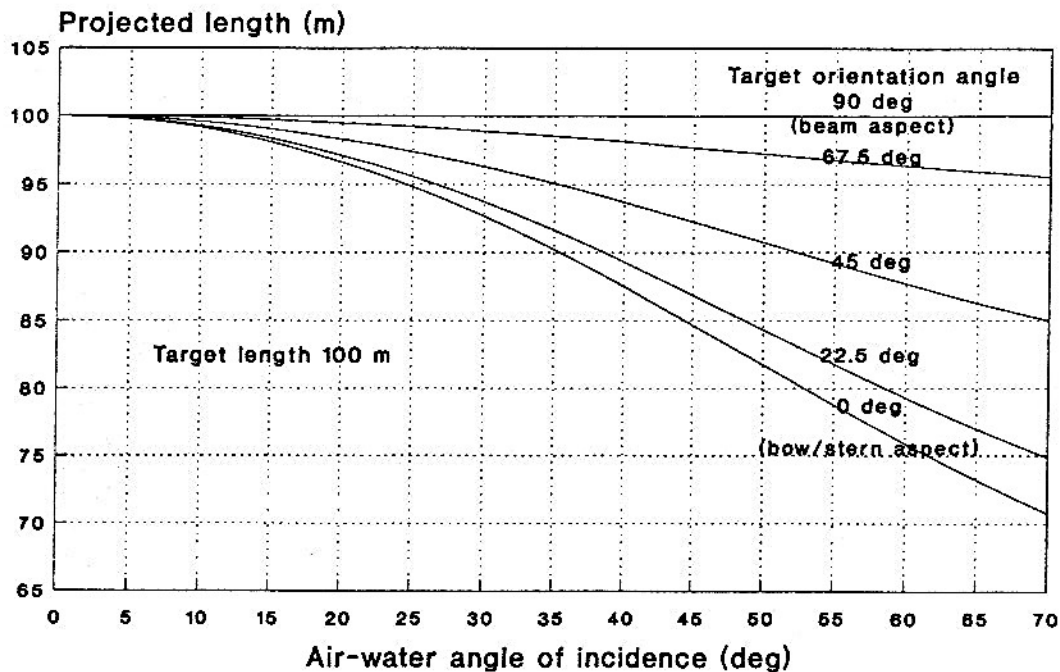
Projected length (m)

Figure 9. Projected length of a horizontal submerged target as a function of angle of incidence for five target orientations.

Geometrical Form Factor

Very often the target may intercept only a fraction of the laser beam. The geometrical form factor F is the ratio of the beam power incident on the target to the total beam power in the plane that is perpendicular to the beam at the location of the target. In this model, it is assumed that the power density is uniform across the beam cross section, at least out to the radial distance from the centerline of the beam that contains 50% of the beam power. From the point of view of geometrical form factor, it is further assumed that if the center of the beam strikes anywhere on the target, the result is equivalent to the beam's striking the center of the target; on the other hand, if the center of the beam misses the target, the entire beam is considered to have missed the target completely. (From the point of view of counting the number of hits on target, it is not necessary for the center of the beam to strike the target as discussed in the development of equation (12).)

21

The geometrical form factor F can be expressed in terms of the area of the target that is common with the cross-sectional area of the beam. Two cases are considered: a cylindrical target, approximating a submarine; and a spherical target, approximating a mine.

If the target is a cylinder of projected length l_p and diameter w, for which $l_p \geq w$, and if the beam has a diameter D_{sp}, it is necessary to consider four cases, depending on the relative values of l_p, w, and D_{sp}. These four cases are illustrated in figure 10.
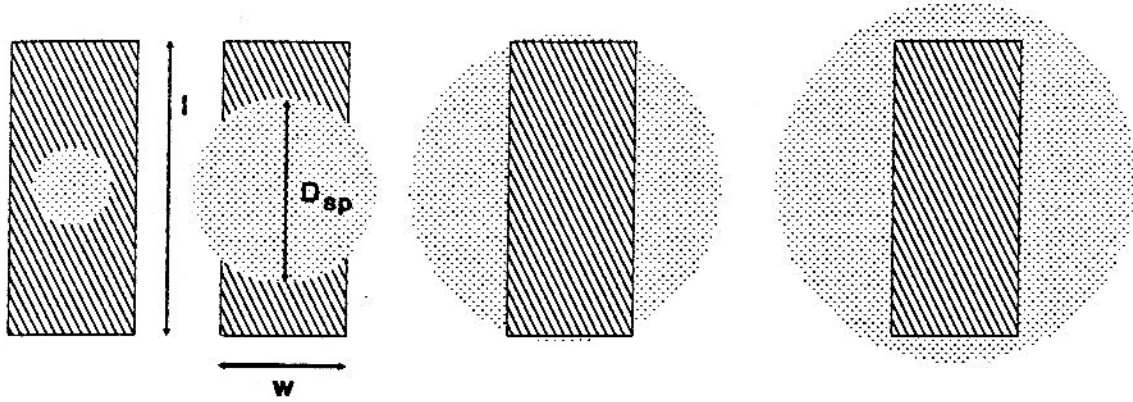
Figure 10. Area of a rectangular target common to circular laser spots of four different diameters.

Case I. $D_{sp} \leq w$

Common area $A_1 = (\pi/4) D_{sp}^2$.   (29)

Case II. $w \leq D_{sp} \leq l_p$

Common area $A_2 = 0.5 (\beta D_{sp}^2 + w D \cos \beta)$ (30)

where $\beta = \arcsin (w/D_{sp})$.

Case III. $l_p \leq D_{sp} \leq (l_p^2 + w^2)^{0.5}$

Common area $A_3 = 0.5 (wD_{sp} \cos \beta + l_p D_{sp} \sin \alpha + [\beta-\alpha] D_{sp}^2)$ (31)

where $\beta = \arcsin (w/D_{sp})$ and $\alpha = \arccos (l_p/D_{sp})$.

22

<u>Case IV.</u> $D_{sp} > (l_p{}^2 + w^2)^{0.5}$

$$\text{Common area } A_4 = l_p w. \tag{32}$$

If the target is a sphere of diameter d_T and the beam has a diameter D_{sp} at the location of the target, it is necessary to consider two cases, depending on the relative values of d_T and D_{sp}. These two cases are illustrated in figure 11.
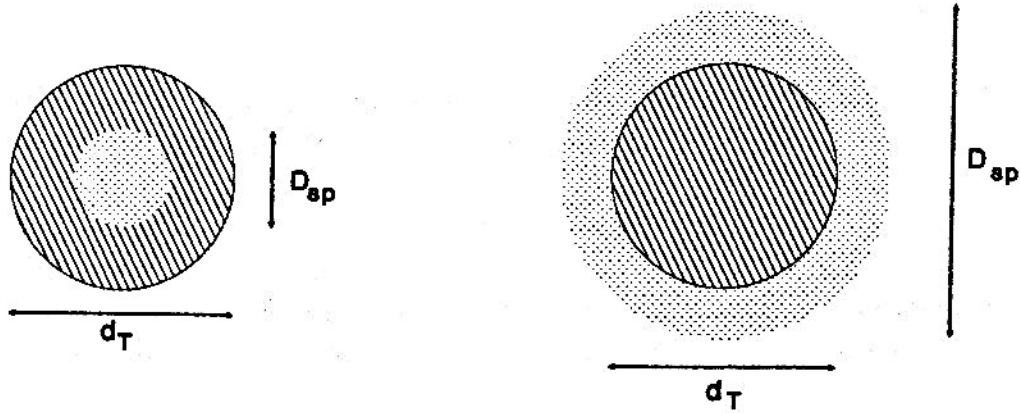
Figure 11.   Area of a circular target common to circular laser spots of two different diameters.

<u>Case I.</u> $D_{sp} \leq d_T$

$$\text{Common area } A_5 = (\pi/4) \, D_{sp}{}^2. \tag{33}$$

<u>Case II.</u> $D_{sp} \geq d_T$

$$\text{Common area } A_6 = (\pi/4) \, d_T{}^2. \tag{34}$$

The geometrical form factor F is then given by

$$F = 0.5 \, A_m / A_{sp} \tag{35}$$

in which m = 1, 2, 3, 4, 5, or 6 as appropriate for each of the above cases. In equation (35), the factor 0.5 appears because the circle of area A_{sp} includes only 50% of the power at the target location.

23

Spreading Factor "B" for Light Emerging into Air from Water

Snead, in reference (f), has developed an expression that relates the solid angle $d\Omega$ that contains a bundle of rays from an underwater object to the solid angle $d\omega$ subtended at the water surface by the same bundle of rays in air after refraction at the interface. Snead's expression, converted to the symbols used in this report, is

$$B = d\omega/d\Omega = \frac{(D \cos \theta + n H \cos \theta')(D \cos^3 \theta + n H \cos^3 \theta')}{(H^2 \cos \theta \cos^3 \theta')} \qquad (36)$$

where $\theta' = \arcsin[(\sin \theta)/n]$.

Figure 12 illustrates the behavior of the factor B as a function of angle of observation in air. For very small values of target depth D, equation (34) reduces to

$$B \approx (n^2 \cos \theta')/\cos \theta. \qquad (37)$$

For observations normal to the sea surface (for which both the angle of incidence $\theta = 0$ and the angle of refraction $\theta' = 0$), equation (35) further reduces to $B \approx n^2$.
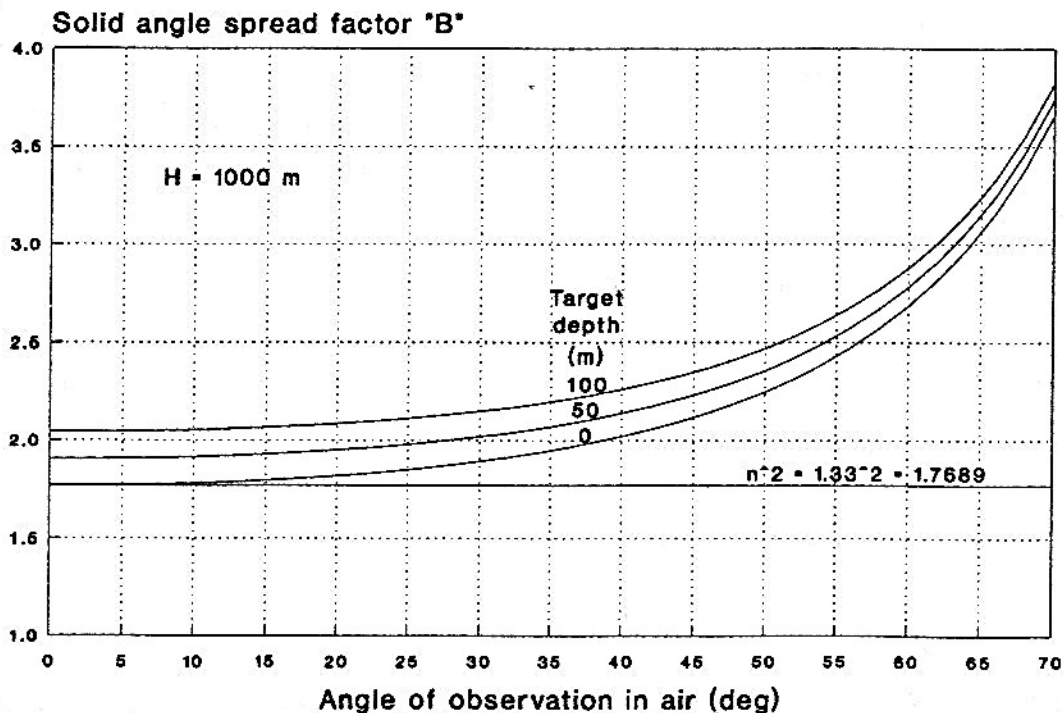
Figure 12. Spreading factor "B" for light emerging into air from under water.

24

Duration of Received Pulse

In general, the received pulse is longer in duration than the transmitted pulse because different parts of the beam, of which the pulse is a part, travel along paths of different lengths in going from the transmitter through the atmosphere and water to the target and back again to the colocated receiver. Pulse "stretching" or "smearing" occurs from a number of causes: (1) path length differences from incidence of a spherical wavefront on the sea surface, (2) differences in effective path length because of oblique incidence at the water surface, (3) differences in effective path length because of surface waves, (4) multiple scattering in the body of the water, (5) path length differences from the incidence of a quasi-spherical wavefront on the surface of the target, (6) path length differences from oblique incidence of light on the target, and (7) reflections off different parts of the target (e.g., rudder, sail, deck) at various ranges from the sensor. In the following treatment, it is assumed that any individual photon travels over the same path to and from the target. Expressions have been developed for calculating the contributions to the received pulse duration t_r over a two-way path from foregoing factors (2), (5) and (6); these three time increments are identified below as t_1, t_2, and t_3, respectively. In all cases it is assumed that the target is a completely submerged right circular cylinder whose longitudinal axis is horizontal and oriented at an angle Γ relative to the plane of incidence of the laser beam.

(1) Oblique incidence at the water surface

Two cases are considered: (1) the effective dimension C_x (defined below) of the target is greater than or equal to the diameter D_{sp} of the incident beam at the target location, and (2) the effective dimension C_x of the target is smaller than D_{sp}. The rationale for the two cases is that if rays of light from both extreme edges of the incident beam (i.e., those that have traveled the greatest and the least distances in air before striking the water surface) impinge on the target, the pulse will be smeared out in time by an amount corresponding to the difference in the two-way distance traveled by the extreme rays. On the other hand, if the target is small compared to the beam diameter at target depth, on any given pulse, the size of the target will determine the extreme rays that actually strike the target; in this case a proportionally smaller spread in path lengths will result.

Let C_x equal the component of target dimension aligned with the horizontal component of propagation vector of the laser light. If l and w are the actual length and diameter, respectively, of the cylindrical horizontal target and Γ is the angle between the longitudinal axis of the target and the plane of incidence of the axis of the laser beam, then

$$C_x = [(l \cos \Gamma)^2 + (w \sin \Gamma)^2]^{1/2}. \qquad (38)$$

25

Case I. $C_x \cos \theta' \geq D_{sp}$

Let t_{1A} equal the two-way contribution to the received pulse duration for the large target situation. Then

$$t_{1A} = (2 \, D_I \tan \theta) \, / \, c. \tag{39}$$

Case II. $C_x \cos \theta' < D_{sp}$

Let t_{1B} equal the two-way contribution to the received pulse duration for the small target situation. Then

$$t_{1B} = (2 \, D_I \, C_x \tan \theta \cos \theta') \, / \, (c \, D_{sp}). \tag{40}$$

The contribution t_1 to pulse smearing from oblique incidence of the laser beam at the water surface is the lesser of t_{1A} and t_{1B}.

(2) Quasi-spherical spreading of the wavefront in seawater

Because of local variations in angle of incidence of the laser light caused by wind-driven surface waves and of multiple scattering of the light in the body of the water, the incident beam increases in diameter from its value of D_I at the surface to D_{sp} at the depth of the target. The wavefront advances with a curvature which is approximately spherical. Even if the center of the wavefront strikes a plane surface at normal incidence, there will be a spread in the distances traveled by different portions of the beam. Three cases, t_{2A}, t_{2B}, and t_{2C}, are considered in arriving at a value for t_2.

Define the size parameter C_p as

$$C_p = l \cos \theta' + w \sin \theta'. \tag{41}$$

Case I. $C_p > D_{sp}$

Let t_{2A} equal the two-way contribution to the received pulse duration for the large target situation. Then

$$t_{2A} = [(2 \, nD \sec \theta')/c]\{\sec[\arctan[(D_{sp}-D_I)(\cos \theta')/(2 \, D)]-1\}. \tag{42}$$

26

Case II. $D_I \leq C_p \leq D_{sp}$

Let t_{2B} equal the two-way contribution to the received pulse duration for the intermediate size target situation. Then

$$t_{2B} = [(2\,nD \sec \theta')/c]\{\sec[\arctan[(C_p - D_I)(\cos \theta')/(2\,D)] - 1\}. \qquad (43)$$

Case III. $C_p < D_I$

Let t_{2C} equal the two-way contribution to the received pulse duration for the small target situation. Then

$$t_{2C} = 0. \qquad (44)$$

The contribution t_2 to pulse smearing from the quasi-spherical spreading of the wavefront in seawater is the lesser of t_{2A} and t_{2B} unless $C_p < D_I$, in which case $t_2 = 0$.

(3) Oblique incidence of light on a horizontal cylindrical target

Two contributions to this pulse-smearing factor are considered: (1) oblique incidence of light along the effective length of the target and (2) incidence upon the curved cylindrical wall of the target, which contributes a two-way increment of path length equal to the diameter of the target.

Let t_3 equal the two-way contribution to the received pulse duration from the combination of these two factors. Two cases, t_{3A} and t_{3B}, are considered in arriving at a value for t_3, depending upon whether the beam diameter at depth is less than or greater than the effective dimension of the target. Thus

Case I. $w \leq D_{sp} \leq l \cos \theta'$

$$t_{3A} = (n/c)\{[2\,D_{sp} \tan \theta' + w \sec \theta' - w] \cos \Gamma + w\}. \qquad (45)$$

Case II. $D_{sp} > l \cos \theta'$

$$t_{3B} = (n/c)\{[2\,l \sin \theta' + w \sec \theta' - w] \cos \Gamma + w\}. \qquad (46)$$

27

The contribution t_3 to pulse smearing from oblique incidence of light on a horizontal cylindrical target is the lesser of t_{3A} and t_{3B}.

(4)   Combined effect of pulse stretching mechanisms

If t_x is the duration of the transmitted pulse, the duration t_r of the received pulse is

$$t_r = t_x + t_1 + t_2 + t_3. \tag{47}$$

Figure 13 illustrates an example of the contributions of each of the pulse-smearing factors. Figure 14 shows an example of how the duration of the received pulse varies with air-water angle of incidence for five values of target orientation angle.

Pulse duration contribution (ns)
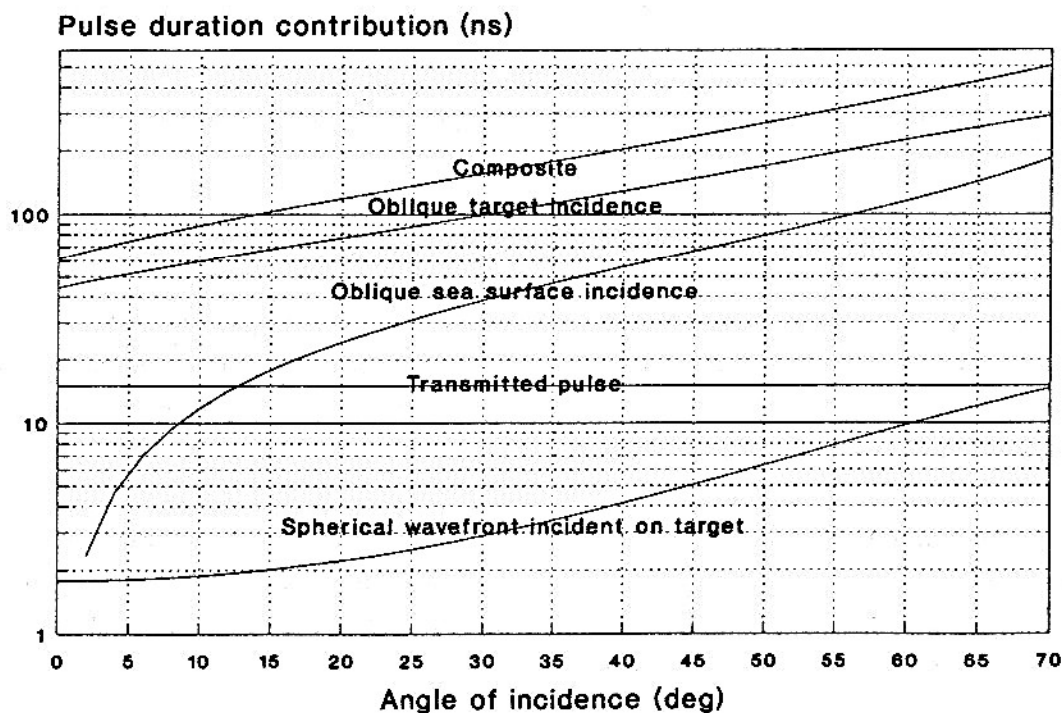
Figure 13.   Contributions to duration of received pulse as a function of air-water incidence angle.

Input parameters: $D = 40$ m, $H = 2000$ ft, $D_I = 10$ m, $\Gamma = 45°$, $l = 100$ m, $w = 10$ m, $K = 0.1/$m

28

Received pulse duration (ns)

Angle of incidence (deg)
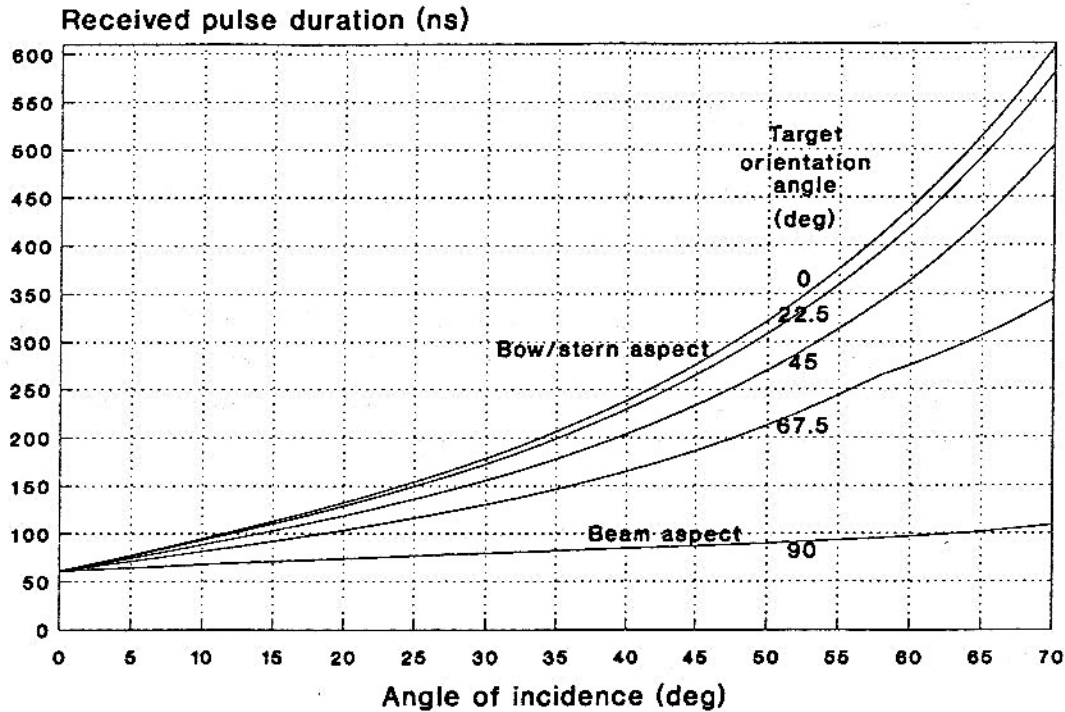
Figure 14. Duration of received pulse as a function of air-water incidence angle for five target orientations.

Input parameters same as for figure 13

Reflectance of a Slab of Water

If laser light reflected from the target is to be detected against a background of laser light backscattered from the bulk seawater in the same range interval as the target, the reflectance of the target must differ from the reflectance of the adjacent slab of seawater. Reference (g) provides values for the diffuse reflectance $\rho_w(\infty)$ as a function of wavelength for long seawater paths that were plotted by Petzold for Jerlov ocean water types I, IA, IB, II, and III. At a wavelength of about 512 nm, Petzold's curves exhibit a "hinge point" and all have the same reflectance value of 0.02. (Data are not provided for the coastal types of seawater.)

If the lidar receiver is gated such that it responds only to returned laser light over a limited seawater path (a relatively thin slab rather than a long column of water) the amount of backscattered light with which the signal from the target must compete is reduced. Reference (g) provides an equation for the range-gated reflectance ρ_w as a function of the

29

range gate time interval τ_g, the attenuation coefficient K, the speed of light c, and the index of refraction of water n:

$$\rho_w = \rho_w(\infty) \; [1 - \exp(K c \tau_g / n)]. \tag{48}$$

The factor in brackets in equation (48) is the fraction of $\rho_w(\infty)$ that is effective in reducing target contrast.

Similarly, if the received signal pulse is smeared out over a time interval t_r, that signal will be in competition with contrast-reducing light backscattered from seawater over the same interval. Thus, equation (48) can be modified to accommodate reflectance from the slab of water corresponding to the duration of the received pulse:

$$\rho_w = \rho_w(\infty) \; [1 - \exp(K c \, t_r / n)]. \tag{49}$$

Forward-Looking Line-Scanning Lidar

For certain applications it may be desirable to direct the look angle of a line-scanning lidar forward. One such situation is one in which the target might be at such a shallow depth that it is not possible to gate out the surface flash. In this case, angling the line scan pattern forward about 15° would eliminate objectionable surface return. A second situation is one in which it is desired to take action (e.g., weapon release) based on lidar information acquired on the same aircraft pass. If the lidar were angled forward say, 45°, a look-ahead distance equal to the aircraft altitude would be achieved, which would translate into time during which action could be taken.

An effect of providing a forward-looking capability is to increase the angle of incidence of the laser beam and the angle from which the return signal is received. If θ_1 is the instantaneous lateral scan angle and θ_2 is the forward look angle, then the resultant angle of incidence θ is given by

$$\theta = \arctan (\tan^2 \theta_1 + \tan^2 \theta_2)^{1/2}. \tag{50}$$

Figure 15 illustrates the variation in θ that results from implementing forward-look angles ranging from 0° to 60° relative to scanning in a vertical plane.
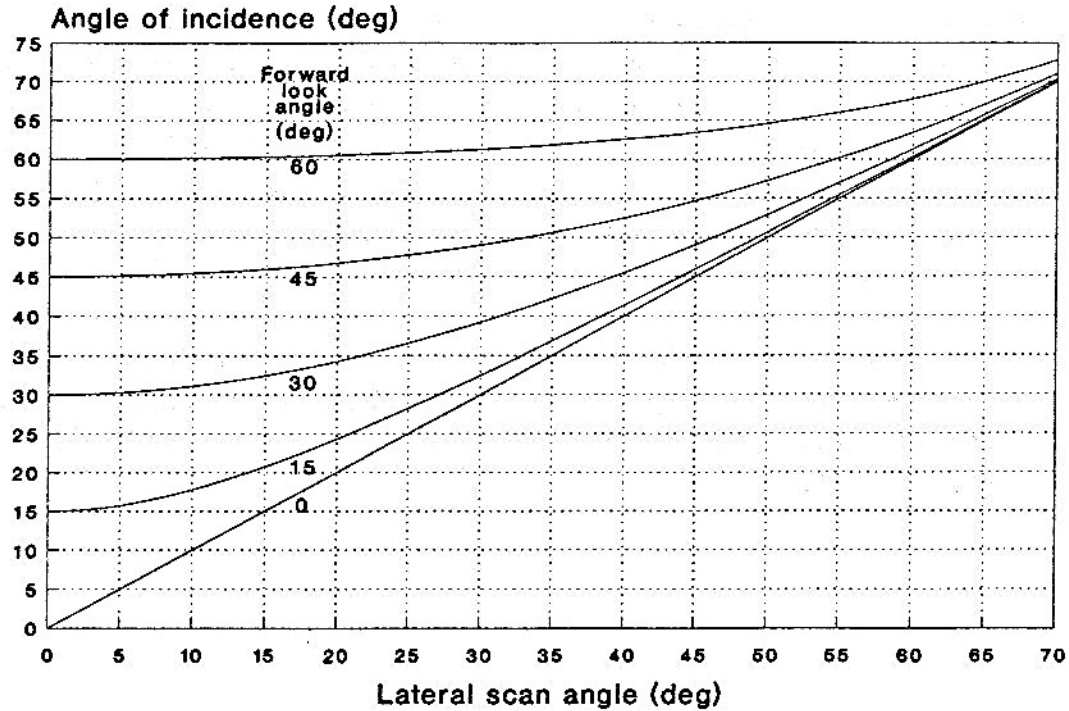
Figure 15. Angle of incidence for a line-scanning lidar as a function of
lateral and forward-look angles.

For a given scanner half angle, the width of the swath swept out increases as the
forward look angle increases. The swath width W is given by

$$W = 2 \, H \tan \theta_m \sec \theta_2. \tag{51}$$

A line scanner has certain advantages over a circular scanner: (1) For all but the end
points of each scan, a line scanner views the surface at smaller (more favorable) angles of
incidence than a circular scanner yielding the same swath width. Indeed, a circular scanner
operates always at a constant, least-favorable angle of incidence. (2) The scanning efficiency
of a line scanner can be higher than that of a circular scanner. (3) For operations during
which the sun or moon is shining, the heading of an aircraft equipped with a line scanner
could be selected to avoid direct viewing of the glare pattern on the surface of the water by
heading into or away from the sun/moon. (4) For a given angular coverage, a line scanner
may not require as large a viewing port (in the fore/aft direction) as a circular scanner.

31

Circular Scanning Lidar

A circular scanner offers the advantage of providing constant resolution and, to a good approximation, uniform detection depth capability throughout the entire scan cycle without the need for varying the laser beam divergence angle, pulse repetition rate, or scan angular velocity during the scan. Because the distance from the sensor to the surface does not vary with position in the scan cycle, gating out surface return is simplified. Because a circular scanner never looks straight down, surface flash problems are mitigated that might occur if surface returns cannot be gated out.

For the model to accommodate a circular scanner, the angle of incidence θ is set equal to the constant scanner half angle θ_m and the scan efficiency is set equal to $2/\pi$ or $1/\pi$ depending, respectively, on whether or not signal integration occurs over both the forward and aft halves of the scan.

EXAMINATION OF CERTAIN PROPERTIES OF THE MODEL

To gain some insight into the various parameters used in the model, the following graphs have been constructed as examples to illustrate magnitudes and dependencies.

Path Length Through Water

Figure 16 is a plot of equation (3). It shows the ratio of path length through the water to depth versus angle of incidence. Although for an angle of incidence of 60° (with respect
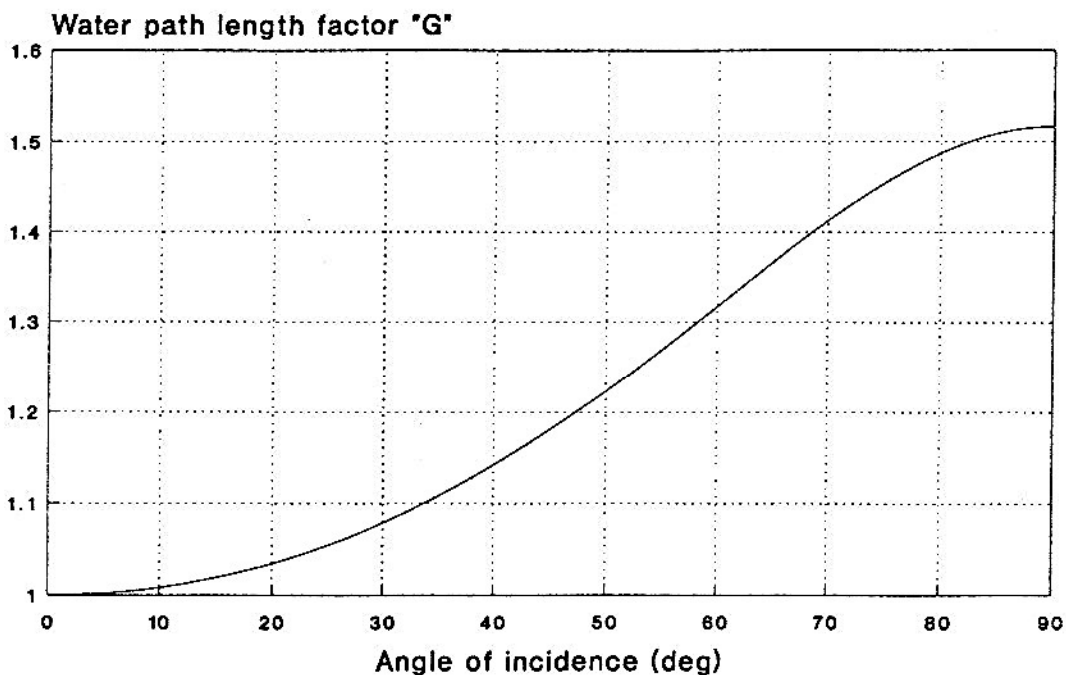
Figure 16. Ratio of path length through water to target depth as a function of angle of incidence.

A "flat earth" was assumed.

to nadir), the path length through the atmosphere is 100% greater than what it is for normal incidence, it is seen that, because of refraction at the interface, the path length through the water to a given depth is only about 32% greater. Thus if one wishes to achieve large area search rates by use of a wide-angle scanner, one would suffer a reduction in detection depth capability because of the larger path length through attenuating water. However, because the wider swath width would be accomplished largely by increasing the path length through the

atmosphere (in which attenuation is relatively small) and because the path length through the water would increase by a significantly smaller amount, the penalties are not as severe as one might initially think.

Effect of Initial Laser Beam Divergence and Sea-Surface Refraction on Laser Beam Diameter

Figure 17 shows the contribution to the laser beam diameter as a function of path length through the water resulting from the initial divergence of the laser beam at the transmitter for the particular case of a 10-m diameter spot at the surface from a vertically downward directed laser at an altitude of 1000 m. Figure 17 also shows the effect of the reduced beam divergence that occurs at the air-water interface as a consequence of Snell's law. This lower curve is a plot of equation (22) for the assumed set of values.
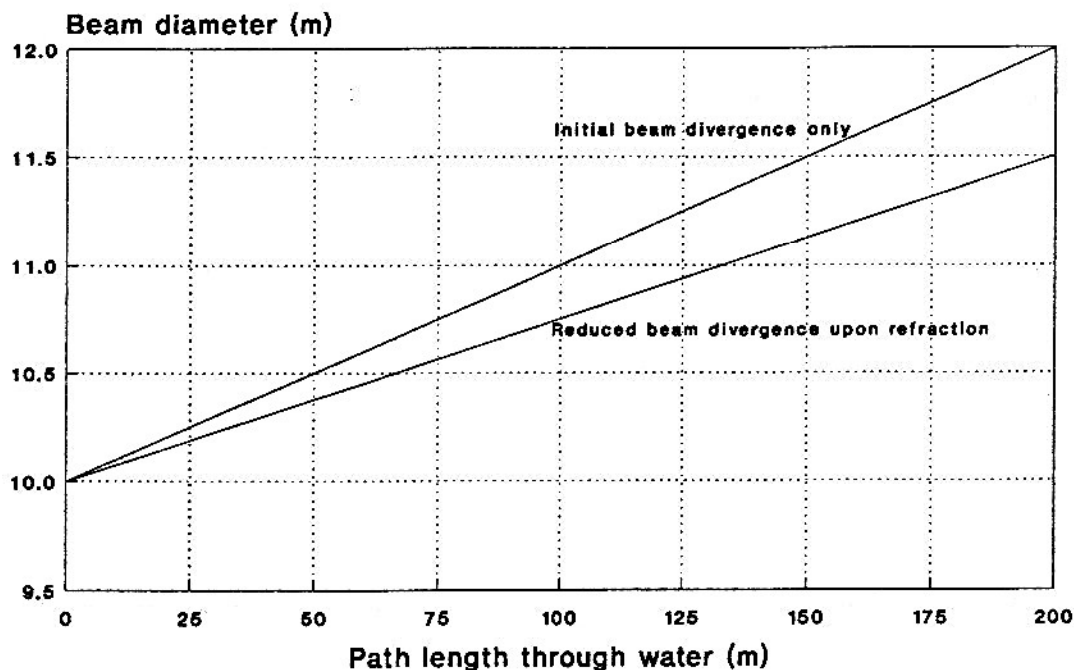
Beam diameter (m)

Figure 17. Contributions to laser beam diameter from initial divergence and from refraction at the sea surface as a function of path length through water.

Effect of Wind-Driven Surface Waves on Laser Beam Diameter

Figure 18 illustrates the contribution D_W to the diameter of the cross section of the beam at the target location from wind-driven surface waves (equation (24)) as a function of path length through the water for three values of surface wind speed. Note that for these

34

wind speeds and for water path lengths of the order of 50 m, this surface roughness contributes about 4 m to the diameter of the beam.

Half-power beam diameter (m)
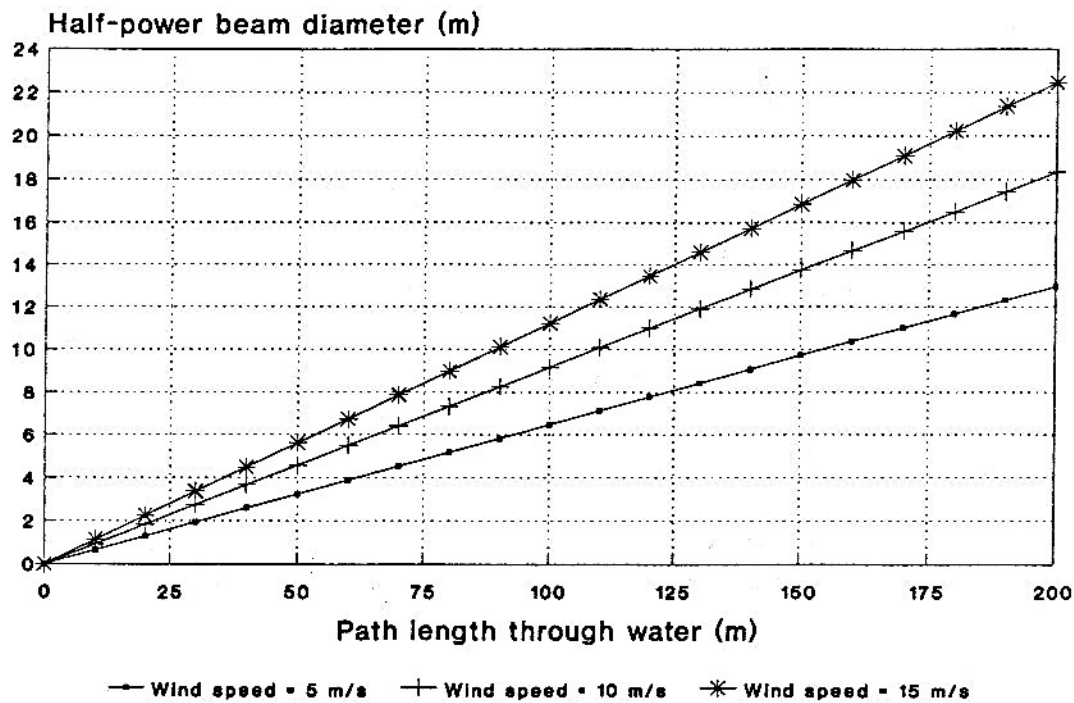
Figure 18. Contribution to laser beam diameter from wind-driven surface waves as a function of path length through water.

Effect of Multiple Scattering in the Body of the Water on Laser Beam Diameter

Figure 19 is a plot of the contribution D_S to the diameter of the cross section of the beam from multiple scattering as a function of path length through the water for five values of diffuse attenuation coefficient K (equation (25)). Note that for water path lengths of the order of 50 m, this scattering in the body of the water may contribute only about 4 m to the diameter of the beam in very clear water and but more than 25 m in the more turbid waters.

Summary of Beam Divergence Effects

Figure 20 summarizes on a single chart the contributions to beam divergence angle described in figures 17, 18, and 19 for one particular set of conditions. In addition, figure 20 shows the composite effect of the three beam divergence mechanisms obtained by applying equation (26).

35

Beam half-power diameter (m)

Path length through water (m)

— K = 0.03/m   + K = 0.05/m   * K = 0.07/m
□ K = 0.10/m   × K = 0.15/m
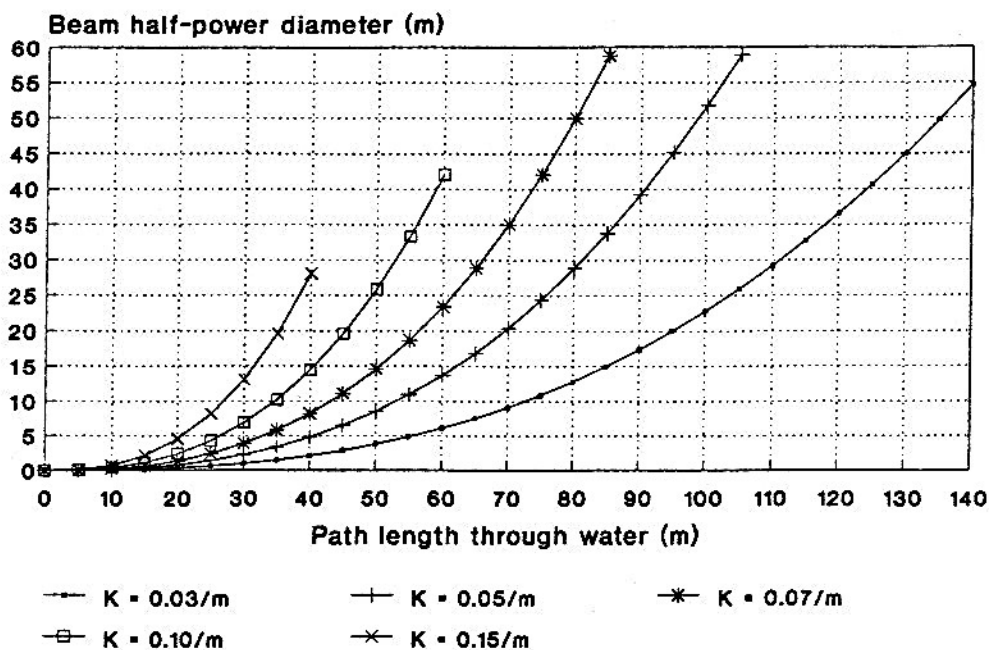
Figure 19. Contribution to laser beam half-power diameter from multiple scattering as a function of path length through seawater for five values of diffuse attenuation coefficient.

Beam diameter (m)

Path length through water (m)

— Diverg after refract   + Surface wave effect
* Multiple scattering   □ Composite effect
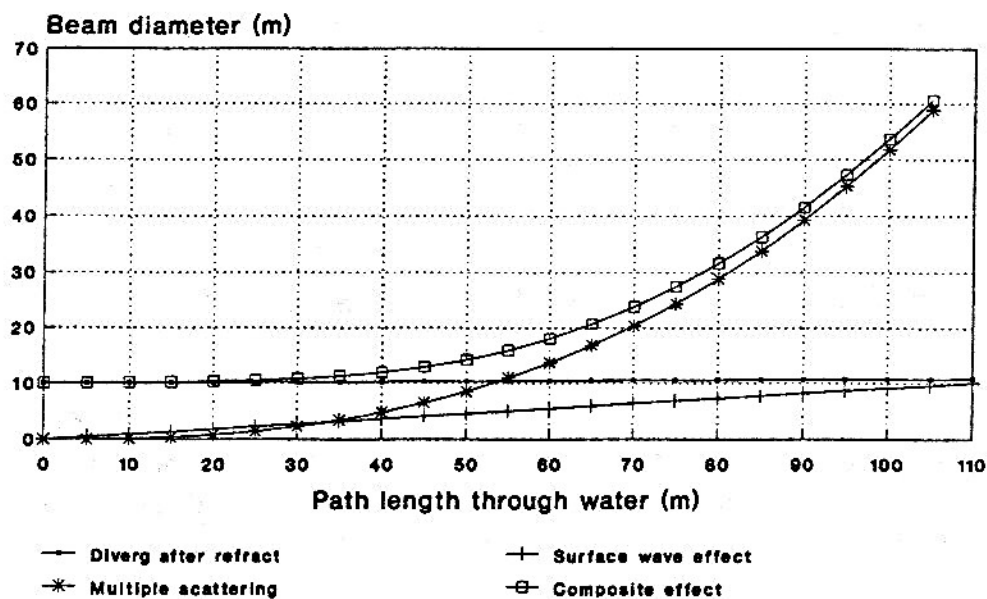
Figure 20. Contributions to laser beam diameter from divergence after refraction, surface wave broadening, and bulk scattering; and root-sum-square composite of these three effects as a function of path length through seawater.

Assumptions: initial beam divergence = 10 mrad; sensor altitude = 1000 m;
K = 0.05/m; wind speed = 10 m/s; normal incidence.

36

Geometrical Form Factor

The geometrical form factor F involves a convolution of the target and the fuzzy spot defined by the laser beam cross section at the location of the target. In this simple model, the target is assumed to be a horizontal right circular cylinder of uniform reflectivity, with its longitudinal axis oriented at an angle Γ relative to the plane of incidence of the laser beam. A "cookie-cutter" type of spot whose diameter is taken as that which includes 50% of the energy of the beam at the target location is used instead of one that might more realistically have a Gaussian distribution. Despite these artificialities, one can still boldly calculate values of F for a wide range of conditions by use of equations (19) through (35).

Values of F were calculated as a function of depth by use of equations (19) through (32) and equation (35) and plotted in figure 21 for six values of surface spot diameter. For depths of less than 25 m, the smallest spot (10-m diameter) fits almost entirely on the target
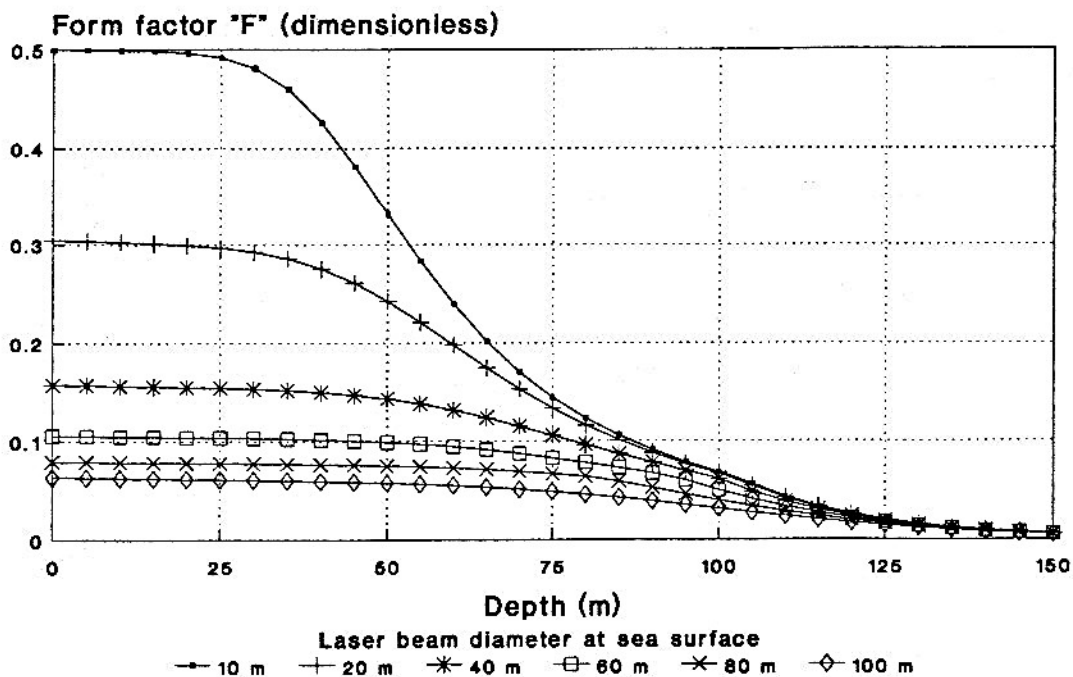
Figure 21. Geometrical form factor "F" as a function of path length through water for six values of laser beam diameter at the sea surface.

Assumptions: K = 0.07/m; sensor altitude = 1000 m; normal incidence; target dimensions = 10 m by 100 m.

37

and F achieves its maximum value of 0.5. With increasing depth, bulk multiple scattering takes over as the principal mechanism determining beam diameter, the curves converge, and beam diameter becomes relatively independent of the beam diameter at the surface. For this assumed set of conditions, it should be noted that a seawater path length of 100 m corresponds to seven attenuation lengths ($K \times D = 0.07/m \times 100\ m = 7$), which probably represents an upper limit of depth performance.

Values of F were calculated for a number of conditions for which values were previously given in reference (a) and compared as a sort of sanity check. (Unfortunately, reference (a) did not provide analytical expressions for beam diameter and geometrical form factor but instead gave only graphical examples.) Figures 22 and 23 are illustrative examples of values of F calculated by use of this model (PSR) and values (ORADS) replotted from reference (a). Calculated results are given for four values of beam diameter at the surface (10, 20, 40, and 60 m) and two values of K (0.05 and 0.10 m^{-1}). In all cases it was assumed that the sensor altitude was 1000 m, the laser illuminated the surface at normal incidence, and the target dimensions were 10 m x 100 m. The agreement appears to be remarkably good, with differences not exceeding a factor of two over depth ranges of practical importance.
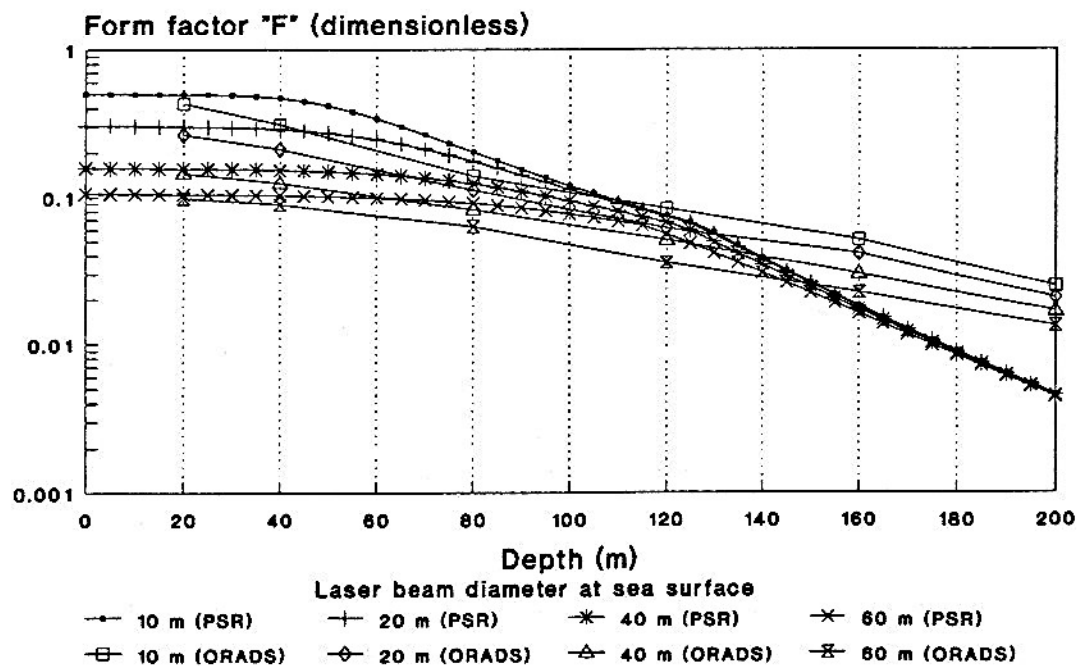
Figure 22. Geometrical form factor "F" as a function of depth and laser beam diameter for K = 0.05/m.

See text for assumptions.

38
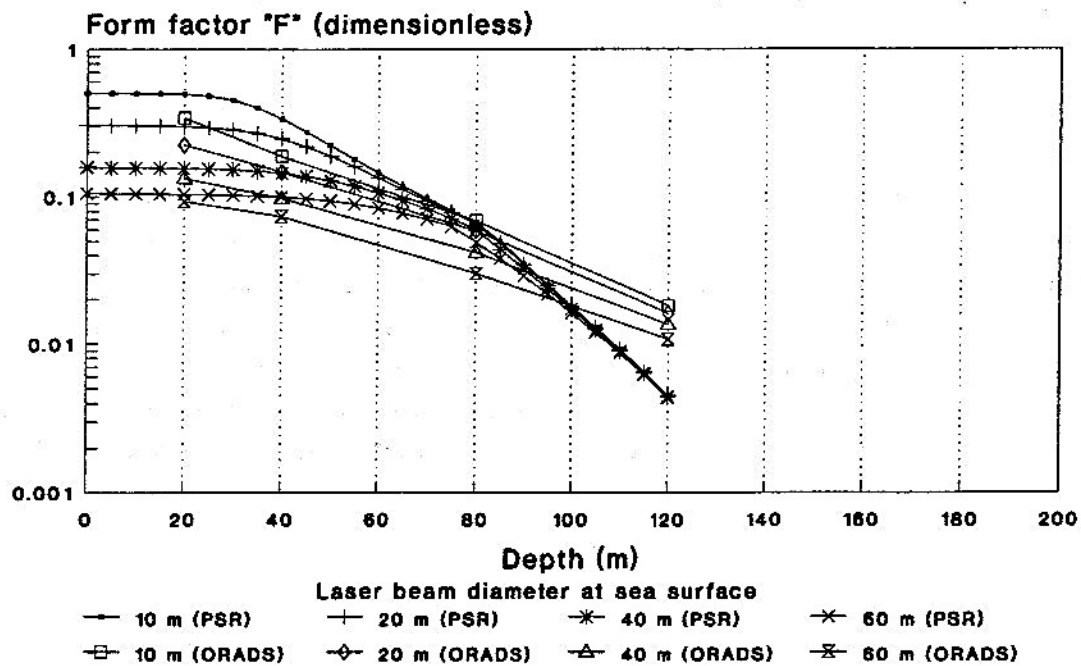
Figure 23. Geometrical form factor "F" as a function of depth and laser beam diameter for K = 0.10/m.

See text for assumptions.

EXERCISING THE LIDAR MODEL

Index of Performance

Equations (14) and (15) have been cast in forms that present the principal sensor parameters on the right side of the equation and the environmental, operational and target parameters on the left side. These equations are used to define what is called, in this report, the "index of performance" which is represented by the symbol I_n or I_d, corresponding, respectively, to the nighttime and daytime situations. The right sides of each equation represent the *available* index of performance and the left sides the *required* or *demand* index of performance. Thus, the available nighttime index of performance is defined as

$$I_n = P_{av} \, e_{sc} \, S \, A_R \, T_R \, T_F \qquad (52)$$

and its units of measure are $A{\cdot}m^2$.

Similarly, the available daytime index of performance is defined as

$$I_d = P_{av} \, e_{sc} \, (S \, A_R \, T_R \, T_F \, / \, \Delta\lambda)^{1/2} \qquad (53)$$

and its units of measure are $m{\cdot}(W{\cdot}A/nm)^{1/2}$.

Design-Performance Tradeoff Assumptions

It is assumed that the parameters constituting I_n and I_d can be traded off in accordance with these equations. For example, for the nighttime case, increasing the photocathode radiant sensitivity S (or, equivalently, the quantum efficiency of the detector) by a factor of two, or doubling the area of the receiver aperture A_R would yield the same improvement in performance as doubling the average power P_{av} of the laser; on the other hand, for the daytime case, a fourfold increase in A_R or S, or reducing the optical filter bandwidth $\Delta\lambda$ to one fourth of its previous value would be required to produce the same effect as doubling P_{av}.

It is further assumed that great flexibility exists in a sensor of given index of performance. Thus it is assumed that a laser transmitter delivering an average output power P_{av} can be made to operate with equal ease at a high pulse repetition rate (PRF) and low energy per pulse or a low PRF and high energy per pulse. Indeed, these could even vary continuously during individual scan cycles. Furthermore, the product of PRF and pulse energy could vary during the scan cycle, as long as P_{av} has its given constant value when averaged over the entire scan cycle. The user is cautioned, after exercising the model, to

check the range of values of parameters tacitly assumed by the model to insure that they fall within the limits of possibility for the current or projected state of the art.

Another caution that must be observed stems from the fact that it is assumed, in the daytime case, that the limiting noise arises from the random arrival of photons at the photocathode from upwelling background radiance originating from the sun, whereas, for the nighttime case, the noise photons originate from the laser. Thus, if one were to reduce the optical filter bandwidth in equation (15) to some very small value (e.g., $\Delta\lambda = 0.001$ nm), one might arrive at the incorrect conclusion that daytime performance of a given lidar could exceed nighttime performance insofar as $\Delta\lambda$ does not appear in equation (14), which covers the nighttime case. When using equation (15) with a very small value of filter bandwidth, one should also perform a calculation with equation (14) to insure that equation (15) does not predict a higher level of performance.

As presently constituted, the model can operate under any of the following three beam management protocols: (1) constant laser beam solid divergence angle, (2) constant beam diameter at the sea surface, or (3) constant spot area on the sea surface. In the latter two cases it is assumed that the beam divergence angle can vary continuously with scanner instantaneous angle of incidence.

Computer Implementations of the Model

The lidar practical performance model was programmed for use on an IBM-compatible personal computer using Lotus 1-2-3 for DOS, Release 2.3. Several Lotus versions of the model have been prepared, each tailored for specific types of computations (e.g., detection depth vs. θ_m, H, and θ; P_{av} vs. θ; nighttime search rate; daytime search rate; circular scanner; line scanner; forward looking line scanner; depth vs. PRF). Because equations (14) and (15) cannot be solved directly for some of the performance measures of greatest interest, such as detection depth and area search rate, graphical or iterative methods must be used. In the graphical approach, one plots the right and left sides of the equation and determines the point of intersection. For example, if one wanted to determine maximum detection depth capability for a given set of conditions, one would fix all values in the equation except depth and then plot the left side of the equation as a function of depth while plotting the right side as a constant.

Detection Depth Capability vs. Indices of Performance

Table 1 is a list of baseline inputs to the model that were assumed in generating the following curves. Figure 24 illustrates the graphical approach for the nighttime case; figure 25 is a similar plot covering the daytime situation.

41

In figure 24, the three curves sloping upward to the right (corresponding to the left side of equation (14)) represent the indices of performance required to achieve a range of detection depths for the conditions stated in Table 1 except that three values of K were used. The three horizontal lines represent three values of available index of performance

TABLE 1. BASELINE PARAMETERS ASSUMED FOR CALCULATIONS

Sensor Parameters

5 W	Laser average power (P_{av})
532 nm	Laser wavelength (λ)
0.12	Detector quantum efficiency (Q.E.)
0.900	Scan efficiency (e_{sc})
15 ns	Transmitted pulse length (t_x)
8 in	Equivalent diameter of receiver optics
0.75	Transmittance of receiver optics (T_R)
0.7	Transmittance of optical filter (T_F)
2 nm	Bandwidth of optical filter $(\Delta\lambda)$

Operational Parameters

Variable	Target depth (D)
2000 ft	Sensor aircraft altitude (H)
85 kn	Sensor aircraft speed (v)
60°	Scanner half angle (θ_m)
30°	Instantaneous lateral scan angle (θ_1)
0°	Line scanner forward look angle (θ_2)
10 m	Laser beam diameter at surface (D_l)
17	Power signal-to-noise ratio (SNR)
45 deg	Target orientation (Γ)

Target Parameters

100 m	Target length (l)
10 m	Target diameter (w)
0.04	Target reflectance (ρ_T)

Environmental Parameters

0.1 m^{-1}	Water diffuse attenuation coefficient (K)
20 km	Atmospheric visibility (R_V)
5 m/s	Surface wind speed (v_W)
0.02	Reflectance of a long column of seawater $(\rho_w(\infty))$
0 (nighttime)	Upwelling background spectral radiance (N_λ)

corresponding to the baseline conditions of Table 1 plus two additional values that are 10 times and 100 times greater than the baseline value. This could be accomplished, for example, by increasing the values of any of the factors (or combination of factors) on the right side of equation (52) by 10 and 100, such as increasing the average power from 5 W to 50 W and to 500 W (as indicated). These three horizontal lines are simply plots of the right side of equation (14). The nine points of intersection of the curves indicate the maximum calculated detection depths achievable under each of the assumed conditions.

Figure 24. Calculated nighttime detection depth capability of baseline lidar for three levels of index of performance I_n and three values of attenuation coefficient.

Note that increases in index of performance by factors of 10 and 100 produce successive increases in detection depth capability of only about 11 m, 8 m, and 6.5 m, respectively, for seawater attenuation lengths (i.e., the reciprocals of K) of 14 m, 10 m, and 7.7 m. This illustrates a rough rule of thumb: one must increase index of performance (e.g., by increasing laser power) by about an order of magnitude to increase the detection depth capability by one attenuation length. Note that increasing any of the other parameters (such as the photocathode sensitivity or area of the receiver aperture) on the right side of equation (14) produces the same result.

In a similar manner, calculations were performed for the daytime case using equation (15); the results are presented in figure 25. The parameters given in Table 1 were used with

43

the exception that the upwelling background spectral radiance N_λ was assumed to be 0.02 $W \cdot m^{-2} \cdot sr^{-1} \cdot nm^{-1}$. (It should be recalled that the definition and units of the daytime index of performance I_d are different from those of I_n.) Relative to the comparable nighttime cases (figure 24), there is a significant decrease in detection depth capability for these daytime cases. Once again, detection depth capability increases by almost one attenuation length for each order-of-magnitude increase in index of performance.

Index of performance increases are not achieved as easily for daytime as for nighttime because most of the parameters on the right side of equation (15) over which one has significant control (except laser power) appear to the one-half power. Thus to increase daytime detection depth capability by about one attenuation length would require a 100-fold
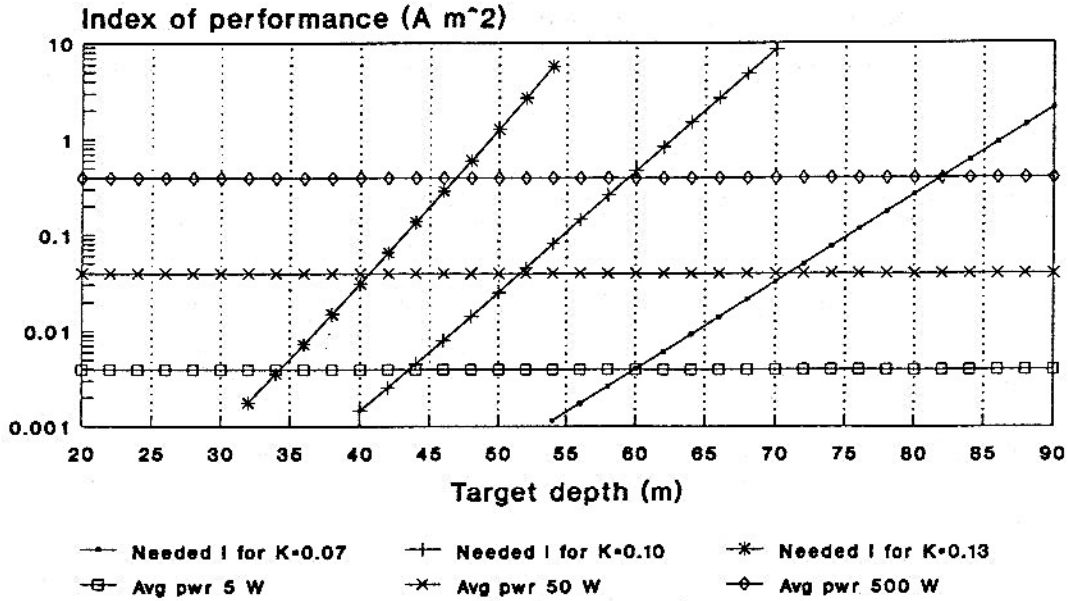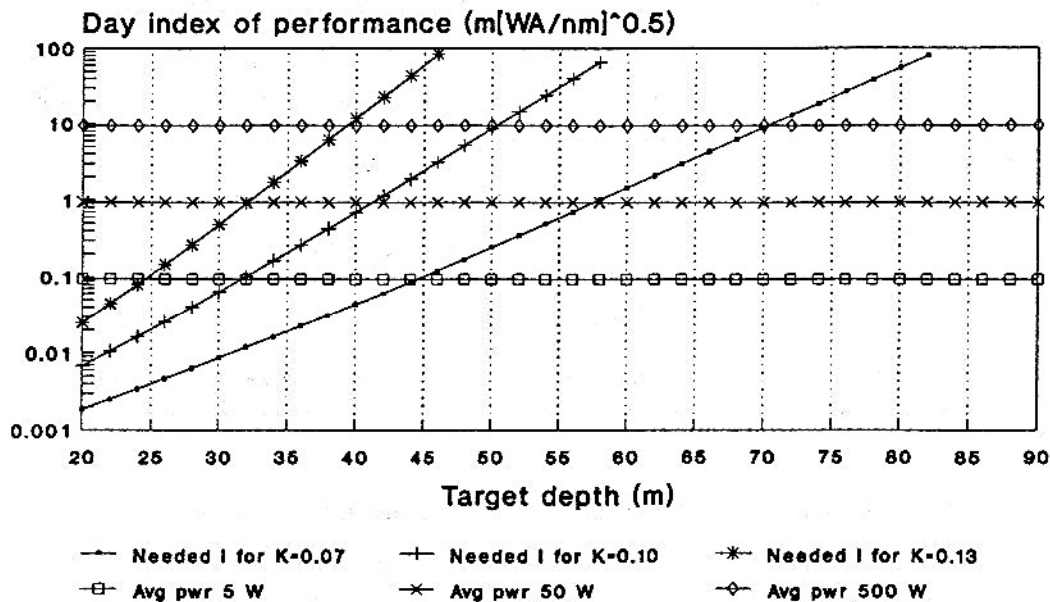

Figure 25. Calculated daytime detection depth capability of baseline lidar for three levels of index of performance I_d and three values of attenuation coefficient.

increase in receiver aperture area or photocathode sensitivity (a practical impossibility because quantum efficiency cannot exceed 1). Reducing the filter bandwidth to 0.02 nm (1% of its previously assumed value) could increase daytime detection depths to a value approaching nighttime values. However, there are practical limits to how narrow the filter bandwidth can be: it should not be narrower than the spectral line breadth of the laser; it must be broad enough to accommodate wavelength instability of the laser; it must be wide enough to enable matching to the wavelength of the laser.

44

Detection Depth Capability vs. Angle of Incidence

The model can be used to explore other dependencies. For example, to calculate detection depth capability as a function of angle of incidence, one can use the same approach as that used to produce figures 24 and 25 but repeat the calculation with the left side of equation (14) or (15) for a range of values of angle of incidence. Such calculations were performed and the results are shown graphically in figure 26. The baseline conditions of Table 1 were used with the following exceptions: calculations were performed for angles of incidence ranging from 0° to 60° in thirteen 5-degree increments; and the diffuse attenuation coefficient K was assumed to be 0.07/m. The point of intersection of each of the "required" index of performance curves with the "available" index of performance line represents the detection depth capability at each of the angles of incidence within the 60-degree-half-angle field of view of the scanner. The seventh ($\theta = 30°$) curve is equivalent to the right most upward-sloping curve of figure 24 and corresponds (as before) to a depth of 60 m. The uppermost curve ($\theta = 60°$) intersects the horizontal line at a point corresponding to 42 m. For a scanner providing lateral coverage of ±60° (i.e., $\theta_m = 60°$) and operating under the assumed conditions, the detection depth capability is greatest near normal incidence (72 m) and drops off gradually with increasing angle of incidence (to 42 m for $\theta = 60°$). Because a constant beam diameter (10 m) at the sea surface was assumed in these calculations, the falloff in detection depth capability is less than if a constant beam divergence angle had been assumed.
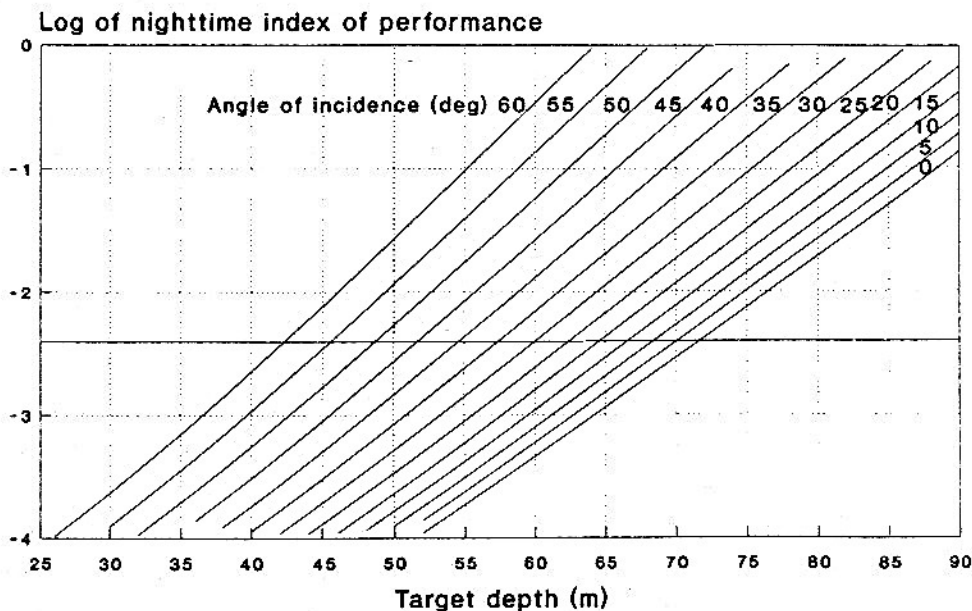
Figure 26. Calculated nighttime detection depth capability for baseline lidar
for angles of incidence ranging from 0° to 60° in thirteen 5-degree
increments.

45

Values of detection depth vs. angle of incidence were effectively read from figure 26 and plotted as the 60° nighttime curve of figure 27. Figure 27 also shows the results of performing similar calculations for lidars with lateral fields of view of ±60°, ±45°, and ±30°
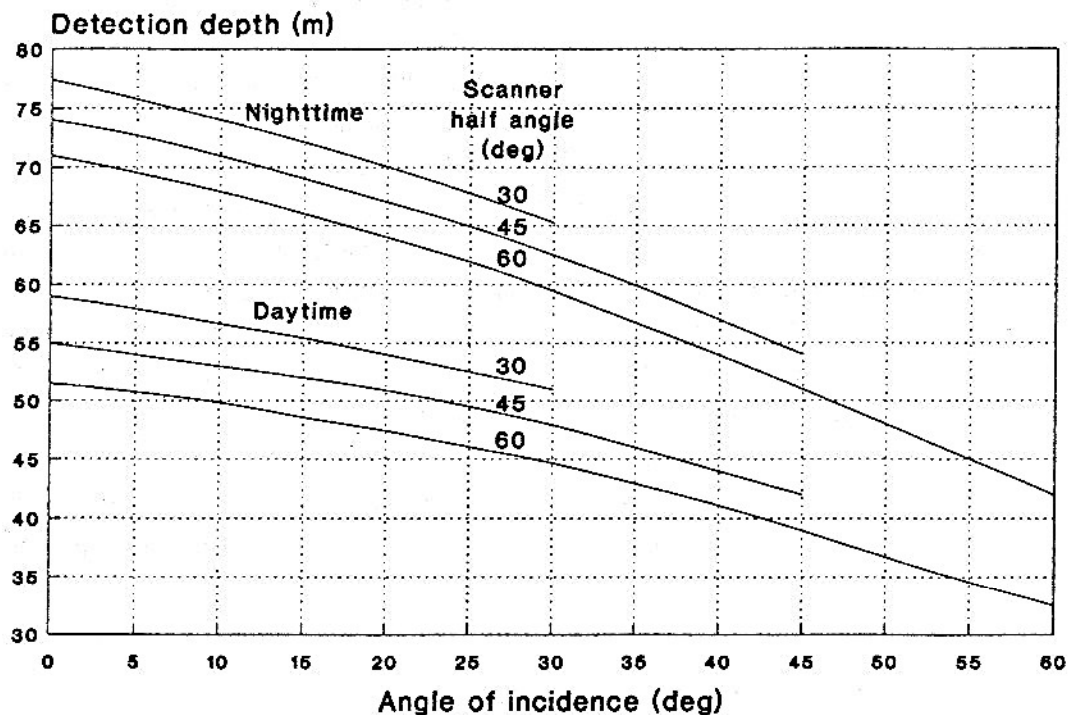
Figure 27. Calculated nighttime and daytime detection depth capability for baseline lidar as a function of angle of incidence for three values of scanner lateral field of view.

See text for assumptions.

(i.e., $\theta_m = 60°$, $\theta_m = 45°$, and $\theta_m = 30°$, respectively) for both nighttime and daytime. Note that (for this particular set of conditions) one gains an increase in detection depth capability of about 3 m by reducing the lateral field of view to ±45° from ±60° and an additional 3 m in reducing the lateral field of view to ±30° from ±45°. These small increases in depth capability are achieved at the expense of large decreases in angular coverage and area search rate. For the assumed aircraft altitude and speed, the surface area search rates for the three angular fields of view (±60°, ±45°, and ±30°) are 96.9, 55.9, and 32.3 nmi²/h, respectively. A factor of three increase in P_{av} (in proportion to the area search rate) would enable a ±60° system to achieve the same detection depth capability as a ±30° system.

46

The same data that were plotted in figure 27 are shown in two alternative ways in figures 28 and 29. In figure 28, detection depth (in ft) is plotted as a function of lateral distance from the sensor flight path within the full lateral fields of view of ±60°, ±45°, and ±30° on a scale that extends to the surface. Figure 28 shows the cross sections (in units of linear distance) of the volume swept out by each of these scanner configurations. Note that the vertical scale is about 16 times greater than the horizontal scale. Consequently, the picture is distorted. This distortion extends to the angles formed by the limiting rays of each
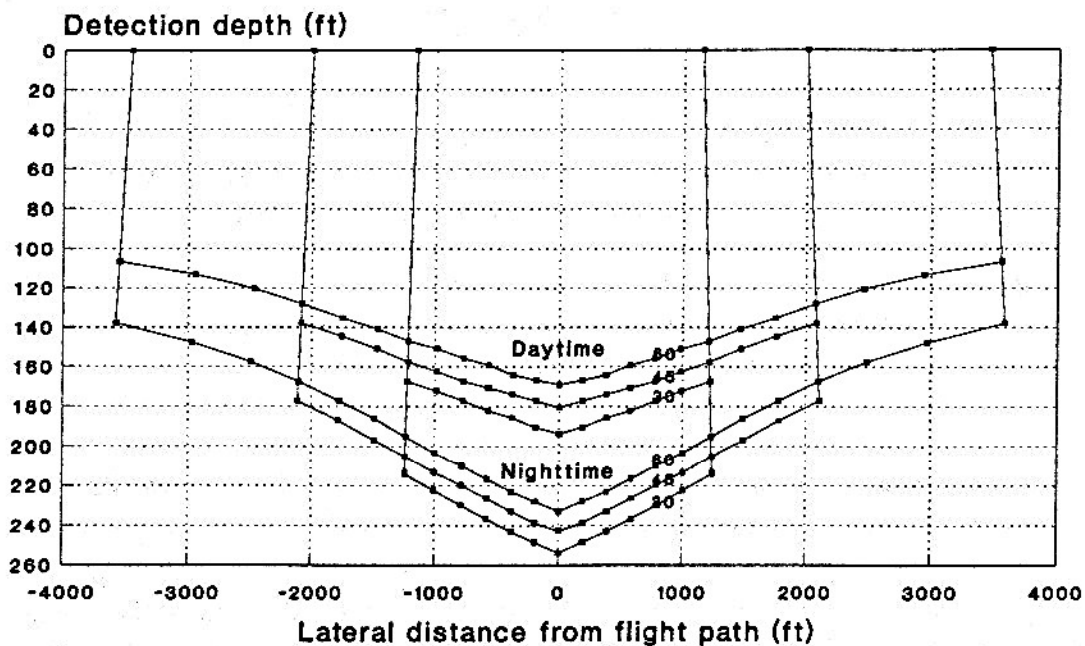
Tick marks are spaced at 5-deg intervals
of incidence angles.

Figure 28. Calculated detection depth and linearized cross-sectional area
swept out by baseline lidar, daytime and nighttime, for three
values of scanner lateral field of view.

See text for assumptions.
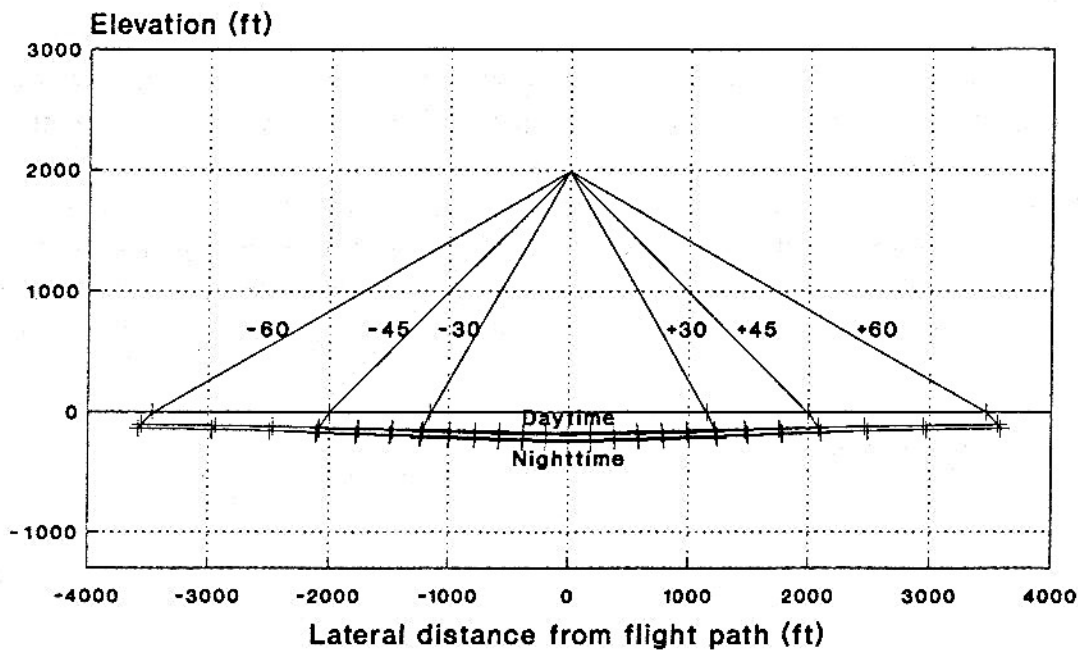
Figure 29. Calculated detection depth and linearized cross-sectional area swept out by baseline lidar, daytime and nighttime, for three values of scanner lateral field of view plotted with equal horizontal and vertical scales.

sector. These rays really deviate from the normal by angles of 40.6°, 32.1°, and 22.1°, the angles of refraction corresponding to incidence angles of 60°, 45°, and 30°, respectively. Not only is the surface area search rate considerably less for the smaller scanner half angles but also the volume search rate is less in almost the same proportion. If the same data are plotted with equal horizontal and vertical scales, the three curves in each of the two sets appear to fall nearly on top of each other as shown in figure 29.

The reduction in depth capability caused by increasing the scanner half angle from 30° to 60°, at any given angle of incidence, is only about 10% (for the particular set of conditions assumed here); however, there is a reduction in depth capability of about 40% as the angle of incidence is increased from 0° to 60° within the ±60° sweep angle. (In figure 28 this amounts to a variation of about ±45 ft relative to the average.) From an operational point of view it may be desirable to "flatten out" the lidar's detection depth capability to avoid holidays in depth coverage. This could be accomplished by increasing the laser energy per unit area on the sea surface with increasing angle of incidence.

Laser "Effective Power" Required for Uniform Depth Capability

One of the parameters that the model allows one to solve for directly is laser average power P_{av}, which is plotted in figure 30 as a function of angle of incidence for three values

48

of diffuse attenuation coefficient K. The baseline parameters given in Table 1 were applied here with the following exceptions: the target deck depth was fixed at 40 m (131 ft); the angle of incidence was allowed to vary between 0° and 60°; K was assigned values of 0.07, 0.10, and 0.13 m^{-1}; the dependent variable P_{av} was allowed to range from about 0.01 W to 10,000 W.

The bottom curve of figure 30 shows that to make the detection depth capability independent of angle of incidence (i.e., a constant 40 m) in fairly clear water (K = 0.07/m), would require P_{av} to vary from 0.019 W (at 0°) to 2.9 W (at 60°) a factor of about 150. As one proceeds to higher values of K, the power required increases by more than an order of magnitude per increment in K; in addition, the power required as a function of angle of incidence increases dramatically with increasing K. For the case of the most turbid water addressed here (K = 0.13/m, corresponding to a clarity between Jerlov's "coastal 1" and "coastal 3"), P_{av} ranges from 4.0 W to 5692 W, a factor of 1423. That is, an enormous increase in power is required to flatten out the depth capability at 40 m with increasing angles of incidence out to 60°, particularly for the higher values of K. Stated differently, a three-order-of-magnitude range in power is required to cope with what would appear otherwise to be a relatively small variation in depth capability. (A similar large increase in power with angle would be required for greater depths D even for the smaller values of K because the product K·D appears in the exponential factor in equations (14) and (15), and because this exponential factor dominates the left sides of these equations.)

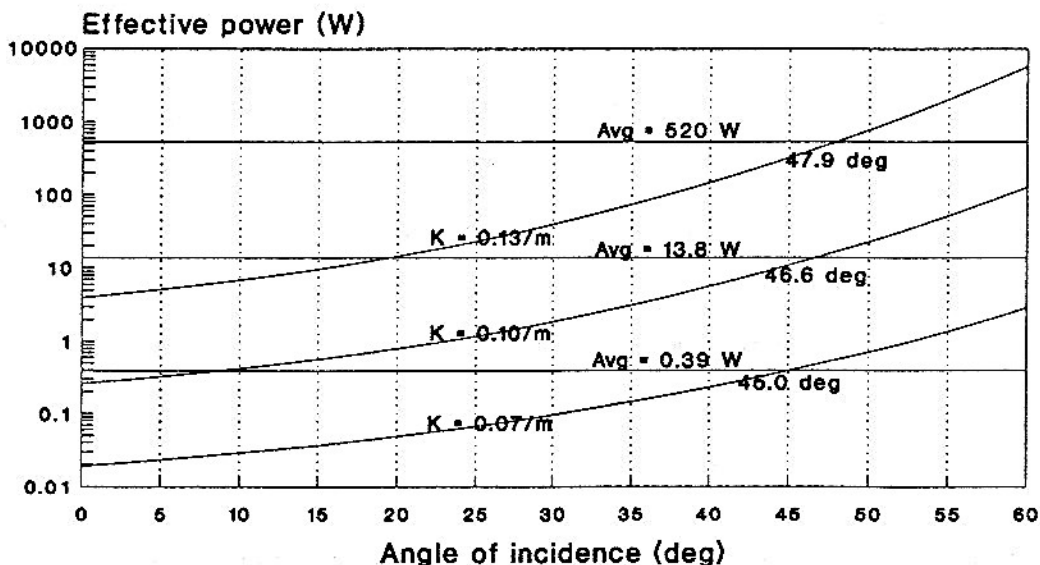
Figure 30. "Effective power" required as a function of angle of incidence for baseline ASW lidar providing a lateral scan angle of ±60° for three values of diffuse attenuation coefficient K and values of each averaged over the entire scan cycle.

See text for assumptions.

49

"Effective Power" Variation Required for Uniform Depth Capability

In exercising the model to determine values such as area search rate vs. target depth, several options are available. For a wide angle system (e.g., 60°), one could perform the calculations assuming an angle of incidence of 0° and arrive at optimistic results. On the other hand, one could assume an angle of incidence of 60° and err on the conservative side. A middle ground is possible, however. One can determine some intermediate angle at which the power required equals the average power over the whole range of angles of incidence. If then, one could "massage" the "effective power" output of the laser to match curves such as those in figure 30, one could still stay within reasonable limits of power averaged over the whole scan cycle.

Average values of power were calculated for each of the three cases illustrated in figure 30 and are displayed as three horizontal lines. For the uppermost curve, for example, the average is 520 W, which corresponds to the power required at an angle of incidence of 47.9°. Similarly, for the other two curves, the averages correspond to the power required at angles of incidence of 46.6° and 45°, respectively. These angles, at which the actual power equals the average power over the scan cycle, range from $0.75\,\theta_m$ to $0.80\,\theta_m$.

Similar computations were performed for scanner half angles of 45° and 30° and for daytime as well as nighttime. An analysis of the results indicates that the angle of incidence θ_N for which the actual power for the nighttime case equals the average power over the full scan of $\pm\theta_m$ can be expressed as

$$\theta_N = F_N\,\theta_m \tag{54}$$

in which

$$F_N = [(\theta_m - 30)\,/\,30]\,[P_N - Q_N] + Q_N \tag{55}$$

where

$$P_N = 0.025309\;K\,D + 0.672720 \tag{56}$$

and

$$Q_N = 0.010932\;K\,D + 0.568081. \tag{57}$$

For the daytime situation, the corresponding angle θ_D can be expressed as

$$\theta_D = F_D\,\theta_m \tag{58}$$

in which

$$F_D = [(\theta_m - 30)\,/\,30]\,[P_D - Q_D] + Q_D \tag{59}$$

50

where
$$P_D = 0.029825\ K\,D + 0.609839 \qquad\qquad (60)$$

and
$$Q_D = 0.012527\ K\,D + 0.542952. \qquad\qquad (61)$$

Equations (54) and (58) are plotted in figures 31 and 32, respectively, for six values of the product $K\,D$. Note that for small values of θ_m, for which the required power varies nearly linearly with angle, the angle of incidence for which the required actual power equals the average power over the entire scan cycle is one half the scanner half angle θ_m. As one goes to larger scanner half angles, especially for the greater values of $K\,D$, the incidence angle corresponding to the average power over the scan cycle increases to about 80% of θ_m.
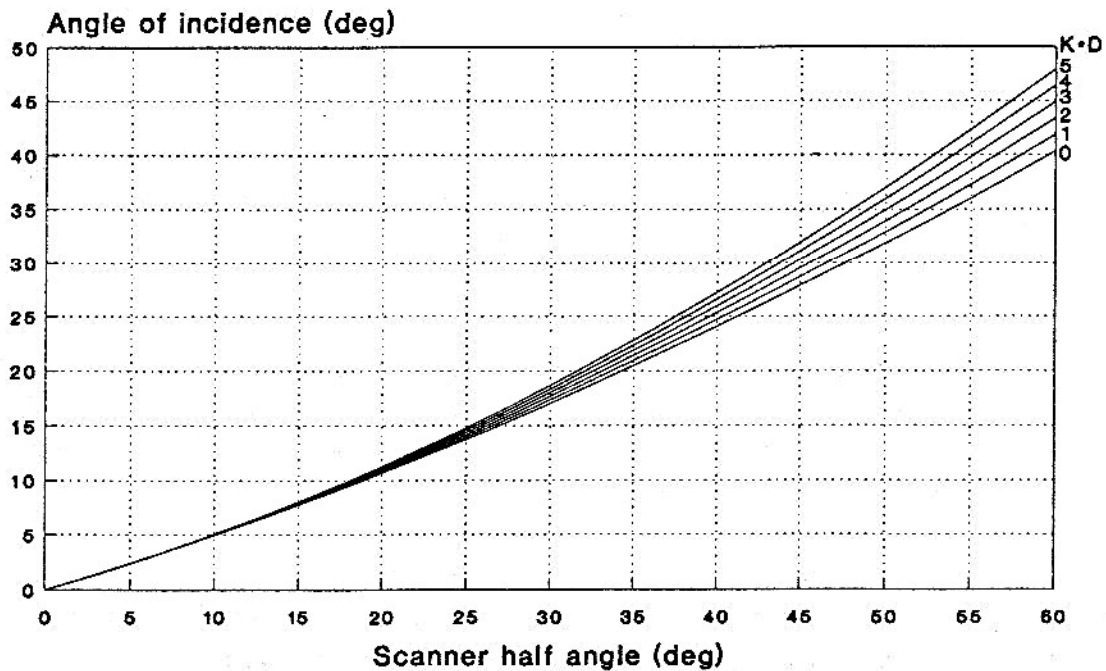
Figure 31.   Angle of incidence at which the instantaneous power equals the average power over the entire scan during nighttime.

51
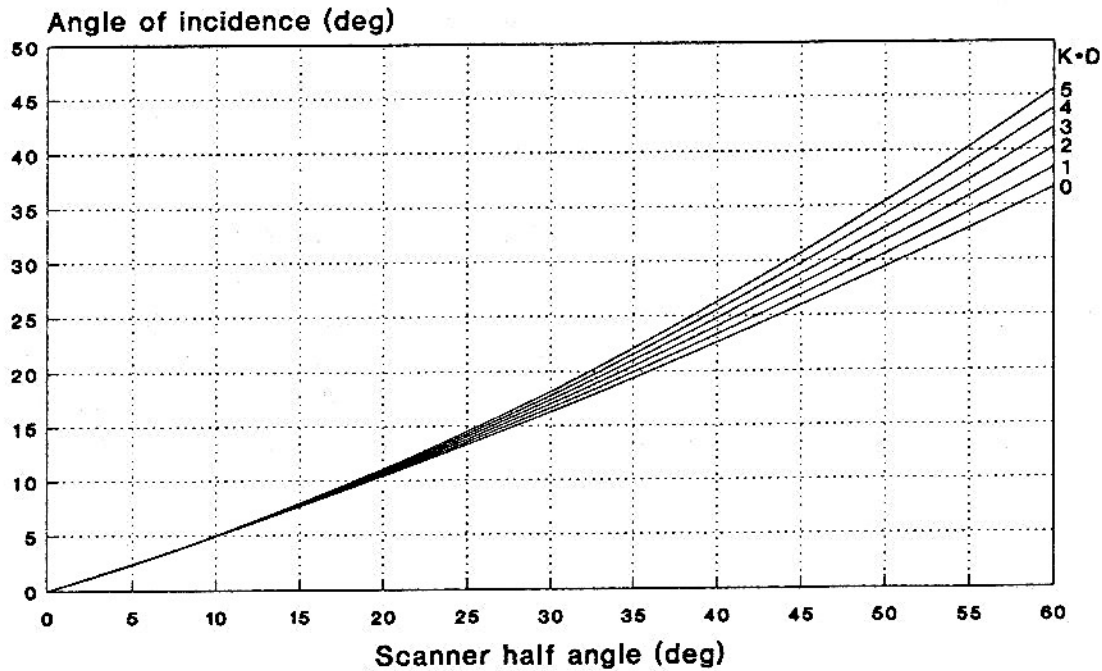
Figure 32. Angle of incidence at which the instantaneous power equals the average power over the entire scan during daytime.

The foregoing demonstrates that, in performing certain calculations with the model in which "effective power" is adjusted as a function of angle of incidence to provide uniform detection depth capability, one can perform the calculations for a fixed ratio of angle of incidence to scanner half angle for any given K D product.

Equations (54) through (61) apply only to line scanning lidars that view the sea surface in a vertical plane; for a forward-looking line scanner, the variation in required power as a function of lateral scan angle is smaller because the range of angles of incidence is smaller. A more rigorous, alternative approach to achieving uniform depth capability (i.e., independent of angle of incidence) would be to calculate, for each application of the model, the power required as a function of lateral scan angle (as illustrated in figure 30), determine its average value, normalize the average power required to the average power available, scale the variable input power accordingly, and input the variable power into the model for calculations of area search rate and swath width.

In the foregoing, it has been assumed that the "effective power" can be varied continuously as a function of angle of incidence. In future USW lidar systems, it should be possible to program the laser to provide a density of luminous energy on the surface of the

water that varies as a function of incidence angle and matches curves such as those shown in figure 30 to provide uniform detection depth capability regardless of where the target appears within the lidar's lateral field of view. The energy density could be increased at the larger angles of incidence in a number of ways: the angular velocity of the scanner could be reduced; the laser pulse repetition rate could be increased; the energy per pulse could be increased; the laser beam divergence angle could be reduced. In exercising certain functions of the model, it is assumed that the laser can operate at some "continuous duty" level of "average power" over the entire scan cycle but that within a scan cycle, the "effective power" may vary over several orders of magnitude. The "effective power" may be varied by any combination of the factors stated above.

Detection Depth vs. Target Orientation Angle

As the angle between the longitudinal axis of the target and the plane of incidence of light from the lidar varies from 90° (broadside, beam aspect) to 0° (bow or stern aspect), two factors conspire to reduce the detection depth capability: (1) the effective target cross section (projected area) of the foreshortened target is reduced, resulting in a smaller return signal, and (2) because the laser pulse strikes the target more obliquely, the duration of the received pulse is increased, resulting in a "smeared-out" signal that is less able to compete with backscattered light from the surrounding sea water within the same range interval.

Figure 33 illustrates the dependence of detection depth capability on target orientation for four viewing angles under the baseline conditions of Table 1. If the target is directly below a line-scanning lidar whose plane of incidence is vertical (zero angle of incidence), the detection depth capability is independent of target orientation. However, if the target is off the sensor aircraft's flight path by amounts corresponding to incidence angles of 30°, 45°, or 60°, detection depth capability decreases with decreasing orientation angle in addition to decreasing with increasing angle of incidence.
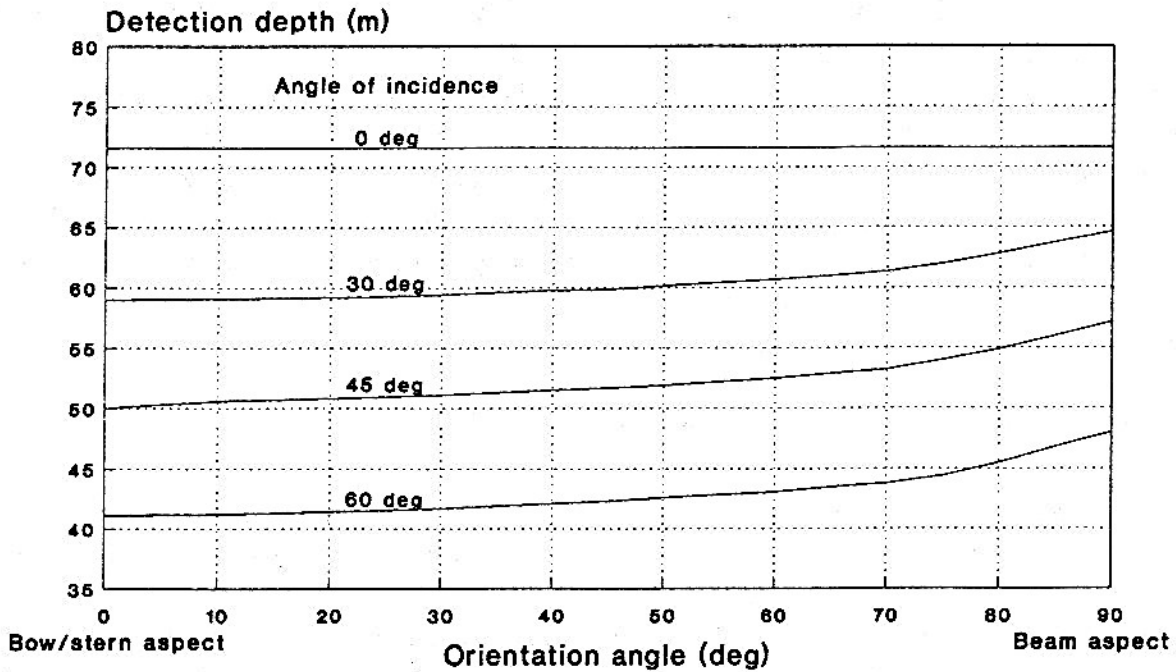
Figure 33. Nighttime detection depth as a function of target orientation angle for incidence angles of 0, 30, 45, and 60 degrees.

Detection Depth Capability of a Forward-Looking Line Scanner

As discussed previously, endowing a line-scanning lidar with a forward-looking capability enables certain advantages in performance and operational utility. However, the achievement of such advantages involves trading off some other performance parameters such as detection depth capability or area search rate.

Figure 34 shows the variation of detection depth capability with instantaneous lateral scan angle for three values of forward look angle. The most extreme reductions in performance appear in close to the flight path of the aircraft, where reductions in depth capability of 7 m and 21 m occur, relative to vertical viewing, for forward look angles of 15° and 45°, respectively. Note, however, that for the 45° forward look case, there is relatively little additional dropoff with increasing lateral scan angle; this is because the angle of incidence varies over a smaller range (from 45° to 63° as shown in figure 15) than for the other two cases.
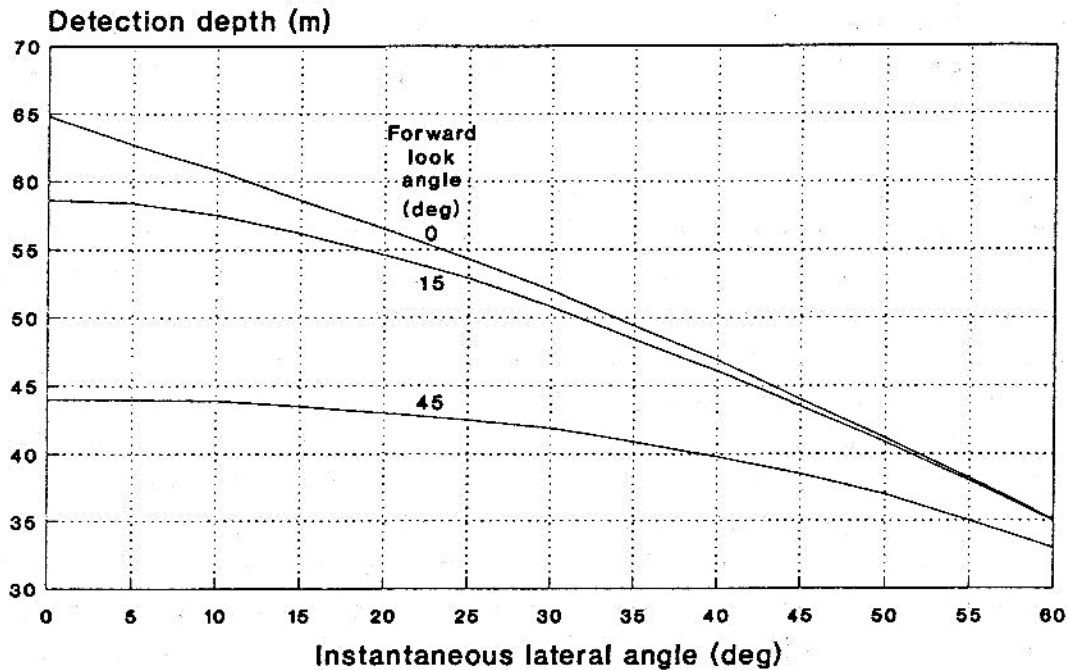
Detection depth (m)

Figure 34. Detection depth as a function of lateral scan angle for a forward-looking lidar of 60° half angle for forward-look angles of 0, 15, and 45 degrees.

Area Search Rate

In a future USW lidar of flexible design, it will be possible to trade off detection depth capability for area search rate. Area search rate $\dot{A}$ is given by

$$\dot{A} = 2 \, v \, H \, \tan \theta_m; \qquad\qquad (62)$$

the ingredients of this equation appear in equations (14) and (15), which describe the possible tradeoffs. Thus there are three ways for increasing (within limits) area search rate: flying faster, flying higher, and increasing the lidar lateral scan half angle θ_m. For a given increase in area search rate, each of these causes a reduction in maximum detection depth; however, the magnitude of the reduction depends upon the method(s) selected. Thus for any given set of circumstances (including aircraft speed), there is an optimum combination of operating altitude and angle θ_m.

It is assumed that future USW lidar systems will be capable of operating with a lateral field of view that is controllable (perhaps over the range of ±10° to ±70°) to yield a maximum area coverage rate for any given set of conditions such as expected target depth,

55

water clarity, sensor altitude, and aircraft speed. For example, if a low-speed sensor aircraft is constrained to operate at low altitude because of a low cloud base but the target is operating in clear, shallow water, it would probably be appropriate to operate with the widest field of view.

Although the Lotus versions of the model enable one to perform a wide range of calculations and provide insight into the effect of changing the various parameters, they do not lend themselves to rapid calculation of certain variables such as optimum sensor aircraft altitude and scanner lateral field of view as functions of, say, target depth, water attenuation coefficient, and aircraft speed. To circumvent the time-consuming "graphical" approach toward solving for certain variables, the model was programmed to obtain solutions through iterative calculations using Borland C++, Version 3.1. Several successive versions were developed, culminating in Laser Performance Model 4.0 (LPM40), which yields results in exact agreement with the Lotus versions. Input parameters are specified by editing a template of a text file LPM4TMP.TXT. LPM40 accepts the input parameters and generates a table consisting of four columns of numbers: scanner half angle (deg), altitude (ft), search rate (nmi^2/h), and swath width (nmi). The program steps through scanner half angles from 0.5° to 70° in 0.5° increments and calculates for each angle the highest altitude up to 10,000 m (32,808.73 ft) that satisfies the input parameters. Search rate and swath width are then calculated for each scanner half angle and corresponding altitude for the specified aircraft speed. Another program, LPM40A, is identical to LPM40 except that it steps through the scanner half angles in 1° increments; the companion input template for LPM40A is LPM40ATP.TXT.

Table 2 is an example of a portion of an LPM40A output file. The data from this file covering the range of half angles from 10° to 70° are plotted as the middle curve of figure 35. This curve illustrates how the maximum area search rate for this given set of operational, environmental, sensor and target parameters varies as a function of sensor altitude and lateral scan half angle. The linear portion of the curve (on the left) represents the geometry-limited situation in which the area search rate is given simply by equation (62)

$$\dot{A} = 2\, v\, H \tan \theta_m = 2 \times 85 \text{ kn} \times H/6080 \text{ nmi} \times \tan 70° = 0.0768 \times H \quad (\text{nmi}^2/\text{h})$$

in which H is in ft in the final expression. Thus, at an altitude of 232 ft, a geometry-limited area search rate of 17.8 nmi^2/h is achieved. As the altitude is further increased, however, the lidar performance becomes sensitivity limited and the lateral scan angle must be reduced to provide the necessary luminous energy density on the sea surface to maintain the 50-m detection depth capability for K = 0.08/m.

TABLE 2. SAMPLE INPUT AND PORTION OF LPM40A OUTPUT

File KDCON2.TXT calculated on (MM/DD/YYYY) 8/11/1994 at 10:52:00

```
************ PACIFIC-SIERRA RESEARCH CORPORATION ***************
******************* WARMINSTER OPERATIONS *********************
************ LIDAR PERFORMANCE MODEL VERSION 4.0A **************
********************* DAYTIME/NIGHTTIME ***********************
************************ 06 JUL 1994 ***************************
******************** INPUT PARAMETERS *************************
```

*** SENSOR PARAMETERS

5.000E+00	(W)	Laser Average Power
5.320E+02	(nm)	Laser Wavelength
1.200E-01	(---)	Detector Quantum Efficiency
9.000E-01	(---)	Scan Efficiency
1.500E+01	(ns)	Transmitted Pulse Length **Used night only
8.000E+00	(in)	Effective Diameter of Receiver Optics
7.500E-01	(---)	Transmittance of Receiver Optics
7.000E-01	(---)	Transmittance of Optical Filter(s) (0<=T(f)<=1)
2.000E+00	(nm)	Bandwidth of Optical Filter(s) **Used day only

*** OPERATIONAL PARAMETERS

5.000E+01	(m)	Target Depth
8.500E+01	(kn)	Aircraft Speed
1.000E+01	(m)	Laser Beam Diameter at Surface
5.000E+01	(---)	Power Signal-To-Noise Ratio
4.500E+01	(deg)	Target Orientation

*** TARGET PARAMETERS

1.000E+02	(m)	Target Length
1.000E+01	(m)	Target Diameter
4.000E-02	(---)	Target Reflectance

*** ENVIRONMENTAL PARAMETERS

8.000E-02	(1/m)	Water Diffuse Attenuation Coefficient
2.000E+01	(km)	Atmospheric Visibility
5.000E+00	(m/s)	Surface Wind Speed
2.000E-02	(1/m)	Reflectivity of Water Slab **Night only
2.000E-02	(W/[m^2-sr-nm])	Upwelling Background Radiance **Day
N	(D/N)	Type of Calculation (Daytime/Nighttime) (D/N)

Angle (deg)	Altitude (ft)	Search Rate (nmi^2/hr)	Swath Width (nmi)
1.0	7588.76	3.704	0.044
2.0	6282.02	6.134	0.072
3.0	5588.24	8.189	0.096
4.0	5123.46	10.017	0.118
5.0	4776.55	11.685	0.127
6.0	4500.60	13.226	0.156
7.0	4271.63	14.665	0.173
8.0	4075.81	16.016	0.188
9.0	3904.49	17.291	0.203
10.0	3751.90	18.498	0.218
11.0	3614.02	19.642	0.231

Search rate (nmi^2/h)

Altitude (ft)

+ D=25 m, K=0.16/m   □ D=50 m, K=0.08/m   ◇ D=75 m, K=0.05333/m

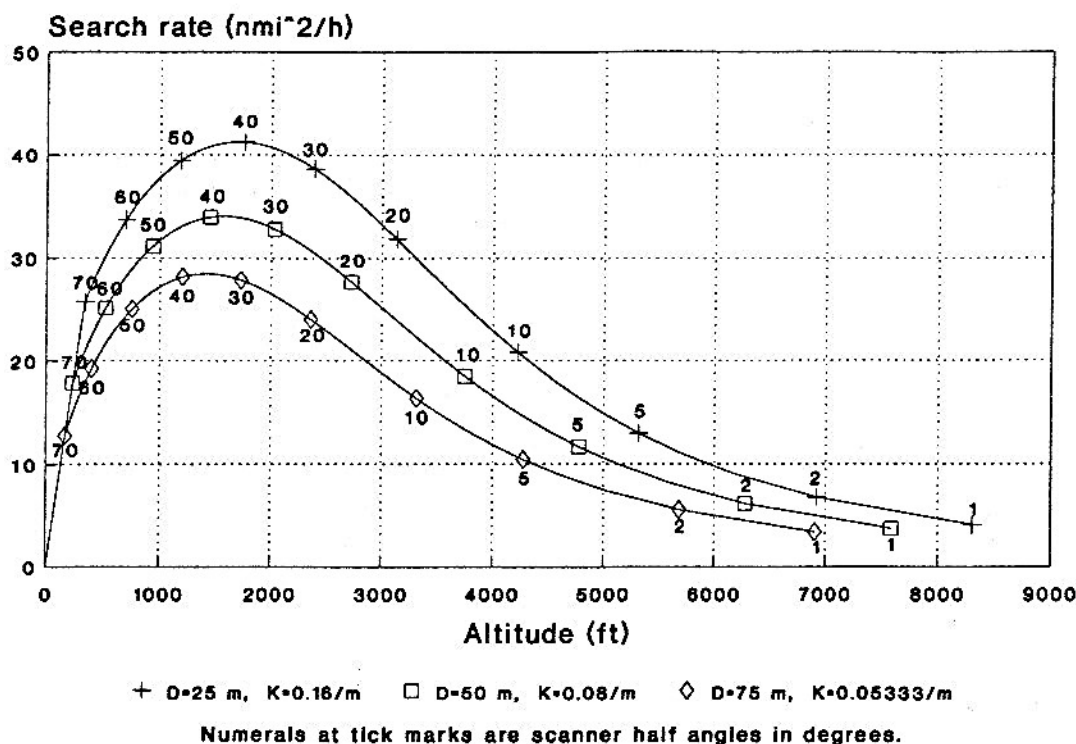Numerals at tick marks are scanner half angles in degrees.

Figure 35. Calculated nighttime ASW lidar search rate as a function of sensor
aircraft altitude and scanner half angle for three combinations of
K and D for which K·D = 4.

See text for assumptions.

For the assumed conditions, a maximum swath width of 0.40 nmi and a maximum
area search rate of 34.0 nmi^2/h are achieved from an altitude of 1559 ft and a scanner half
angle of 38°. As the altitude is further increased, it is necessary to reduce the lateral field of
view further such that the search rate actually decreases with increasing altitude.

Two other curves also appear in figure 35. All three curves were drawn based on the
input values assumed in Table 2 except that two additional values of target depth D (25 m
and 75 m) and two additional values of attenuation coefficient K (0.16/m and 0.05333/m)
were assumed. Thus, for all three curves, the product K·D = 4. (The product "K·D" is often
used as a simple indicator of detection task difficulty and, by extension, of the performance
capability of a USW lidar.) It is seen that, even for a constant K·D product, the area search
rate decreases with increasing target depth. This occurs because the geometrical form factor
F is a function not only of K·D in combination but also of D separately. (See equation (25).)
That is, the increasing depth dominates the diminishing attenuation constant. Thus, to

58

describe a particular lidar as a "K·D = 4 system," for example, has limited meaning, even when search rate is taken into account.

To explore the dependence of area search rate on target depth for a given constant value of attenuation coefficient (K = 0.10/m), the curves of figure 36 were plotted. The
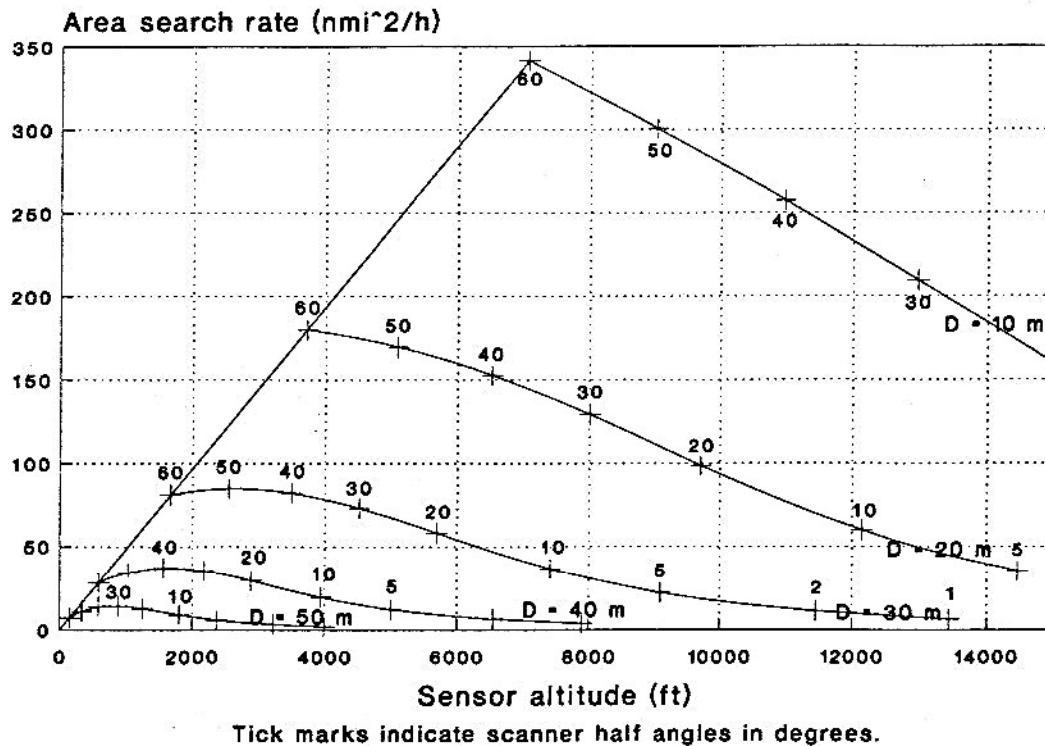

Figure 36. Calculated nighttime ASW lidar maximum area search rate as a function of sensor altitude and scanner half angle for five target depths D.

See text for assumptions.

baseline values given in Table 2 were assumed except that K was taken as 0.10/m and five values of depth were used (10, 20, 30, 40, and 50 m). Once again, the straight line sloping upward to the right represents the geometry-limited situation corresponding, in this case, to θ_m = 60° for all the curves. Note that, for the assumed conditions, the maximum search rate drops off by an order of magnitude in exchange for an increase in detection depth capability from 10 m to about 40 m.

If the lateral field of view of the scanner is constrained to ±60° and the sensor aircraft speed is limited to 85 kn, it is necessary (but not sufficient) to increase the sensor altitude if

large search rates are to be achieved. For example, in figure 36, to realize the large search rate of 342 nmi^2/h for a detection depth capability of 10 m, would require flying the sensor aircraft at an altitude of 7057 ft, which would be unlikely for a helicopter. Furthermore, the sensor must be operated below any cloud base that may exist in the operating area. As an
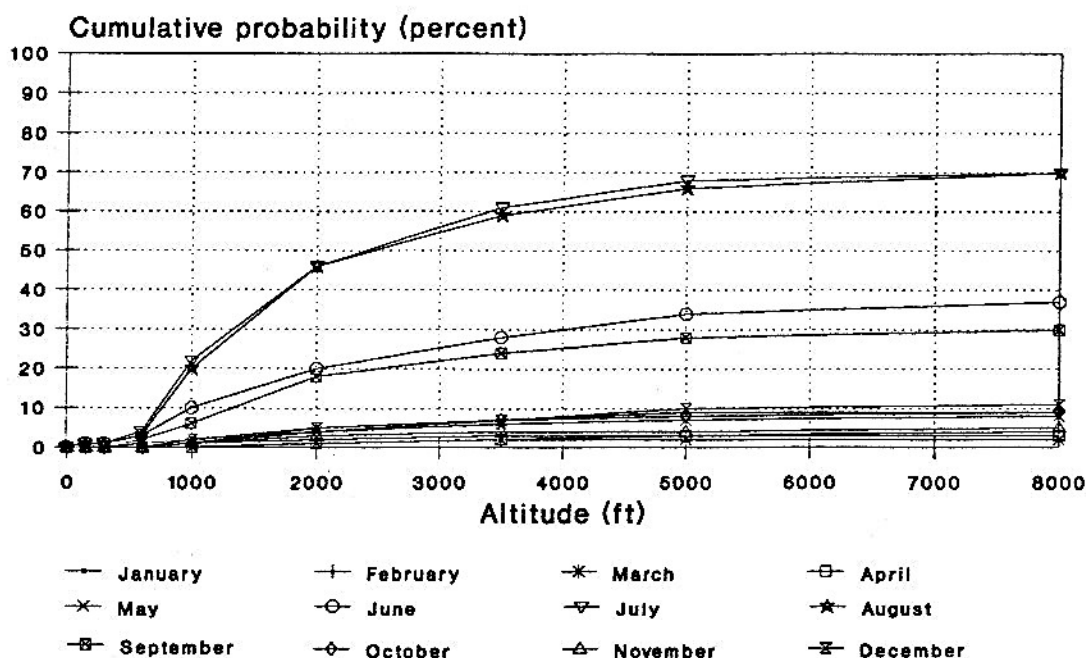

Figure 37. Probability of low cloud ceiling over the Arabian Sea within the area bounded by 16° to 18° N and 64° to 67° E.

A "ceiling" is considered to exist only if the cloud cover ≥ 5/8. Lidar operation could be seriously impaired for even smaller intervening cloud amounts. Data were taken from reference (h).

example of this potential limitation, figure 37 shows the probability of low cloud ceiling over an area of the Arabian Sea for twelve months of the year. For eight of those months, the probability of a ceiling below 8000 ft is less than about 10%, and thus should not interfere seriously with USW lidar operations. On the other hand, for two of the remaining months (July and August), there is a 70% probability that a ceiling exists below an altitude of 8000 ft. During these two months, the highest altitude at which the lidar could operate, with only a 10% probability of a ceiling intervening between it and the surface, would be less than 800 ft. For the conditions assumed in figure 36, if the sensor aircraft is constrained to a 800-ft

60

altitude, the search rate would be limited to about 39 nmi^2/h regardless of whether the assumed target deck depth is 10, 20 or 30 m.

The data used in plotting figure 36 were used in preparing figure 38, which shows, in a different format, the maximum area search rate as a function of detection depth capability along with the corresponding sensor altitudes needed to achieve those search rates. The good news is that one could achieve search rates of over 340 nmi^2/h against a periscope-depth submarine (10-m deck depth); the bad news is that one must be able to fly at an altitude of over 7000 ft to achieve this with a ±60-degree lidar. Increasing the lateral field of view to perhaps ±70° might be a feasible means for addressing the shallow target situation at lower sensor altitudes while still maintaining a high search rate. The model indicates that a ±70° system would yield a 391-nmi^2/h search rate from an altitude of 5088 ft.
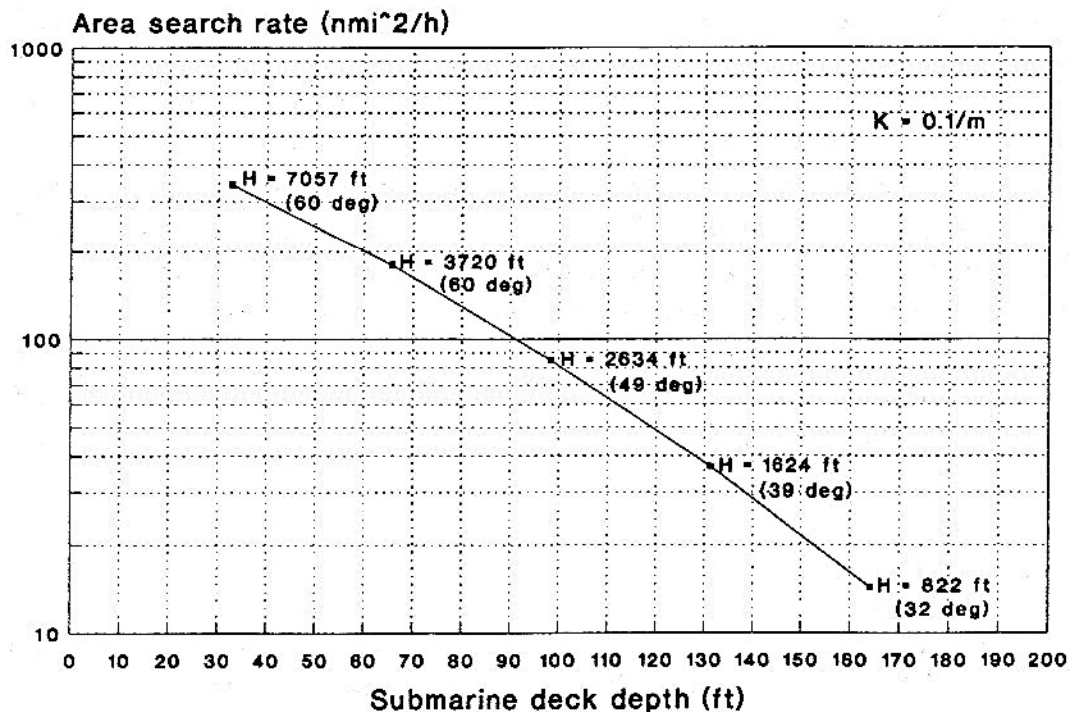

Figure 38. Calculated nighttime maximum area search rate for baseline ASW lidar as a function of target depth for K = 0.10/m.

See text for additional assumptions.

61

Mine Hunting

The model can be used to calculate the performance of lidar for mine hunting, provided the various assumptions made in developing the model are satisfied. The dimensions of the target can be reduced from, say, 100 m by 10 m for a submarine to, perhaps, 1 m by 1 m for a mine. In addition, it would appear appropriate to reduce the diameter of the laser beam at the surface to perhaps 1 m, vice 10 m. (One is cautioned to insure that the laser can provide the required PRF consistent with the smaller beam diameter.) The model tacitly assumes that the target has a water background that is less reflective than the target and that the sea floor is a large distance beyond the target. Thus, it would probably be incorrect to apply the model to a mine (or a submarine, for that matter) resting on the sea floor. It does not appear unreasonable to apply the model in its present form to a moored mine.

Figure 39 provides a comparison of search rates achievable with the baseline sensor operating at night against a submarine and against a mine. The baseline conditions of Table 1 apply except the depth of each target is assumed to be 10 m, the seawater attenuation coefficient $K = 0.15/m$, and the laser spot diameter at the surface is 1 m for an assumed cylindrical mine of diameter and length 1 m. The maximum search rate against the submarine is 275 nmi^2/h which is achievable from an altitude of 3579 ft with a scanner providing lateral coverage of $\pm 70°$. For the mine, the maximum search rate is 45 nmi^2/h from an altitude of 1081 ft. Once again, the straight line sloping upward to the right represents the geometry-limited search rate imposed by the assumption of a $\pm 70°$ lateral field of view. The higher search rate against the submarine stems from the fact that the lidar achieves a significantly greater number of hits of higher luminous energy on the larger target. Of course, if the sensor aircraft is constrained to operate at an altitude of 558 ft or less, the search rate is the same for both targets.

Sensitivity Analyses

The model can be used to explore variations in predicted lidar performance as a function of variations in the operational, environmental, sensor, and target parameters. An example of this would be to determine how accurately one should measure the seawater attenuation coefficient K to enable operating the lidar at its fullest capability for a given set of circumstances. Figure 40 was prepared by exercising the LPM40A version of the model for three combinations of detection depth capability D and attenuation coefficient K. The baseline conditions of Table 1 were assumed except for the values of K and D.
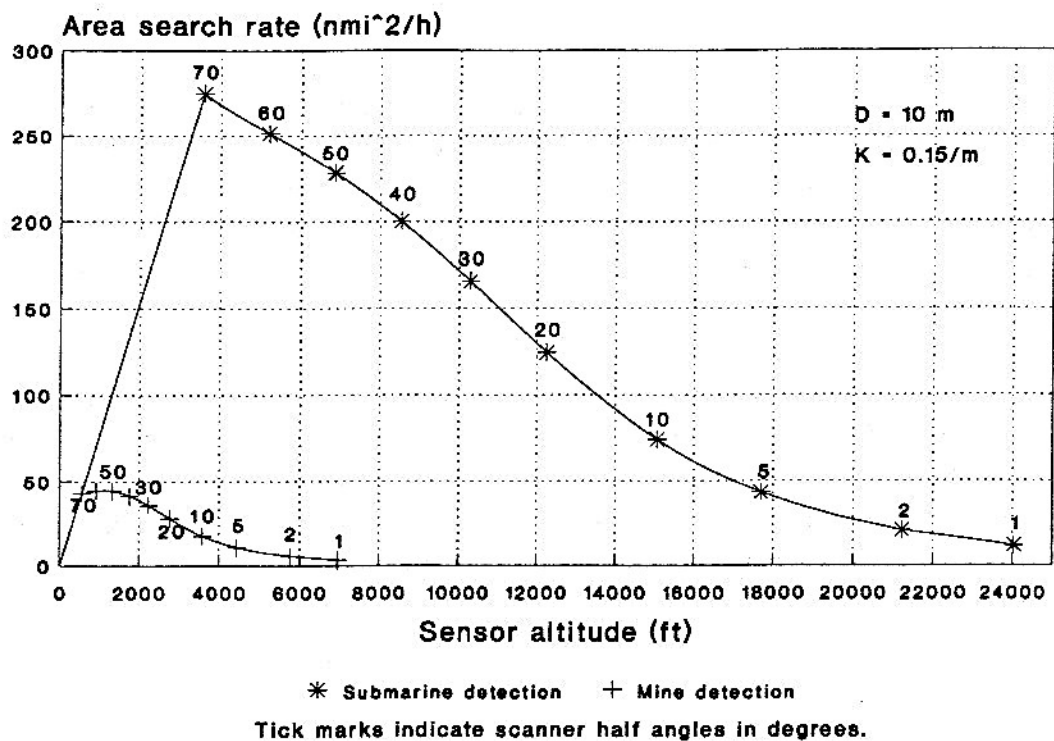
62

Figure 39. Comparison of calculated nighttime area search rates for baseline USW lidar for submarine and mine detection.
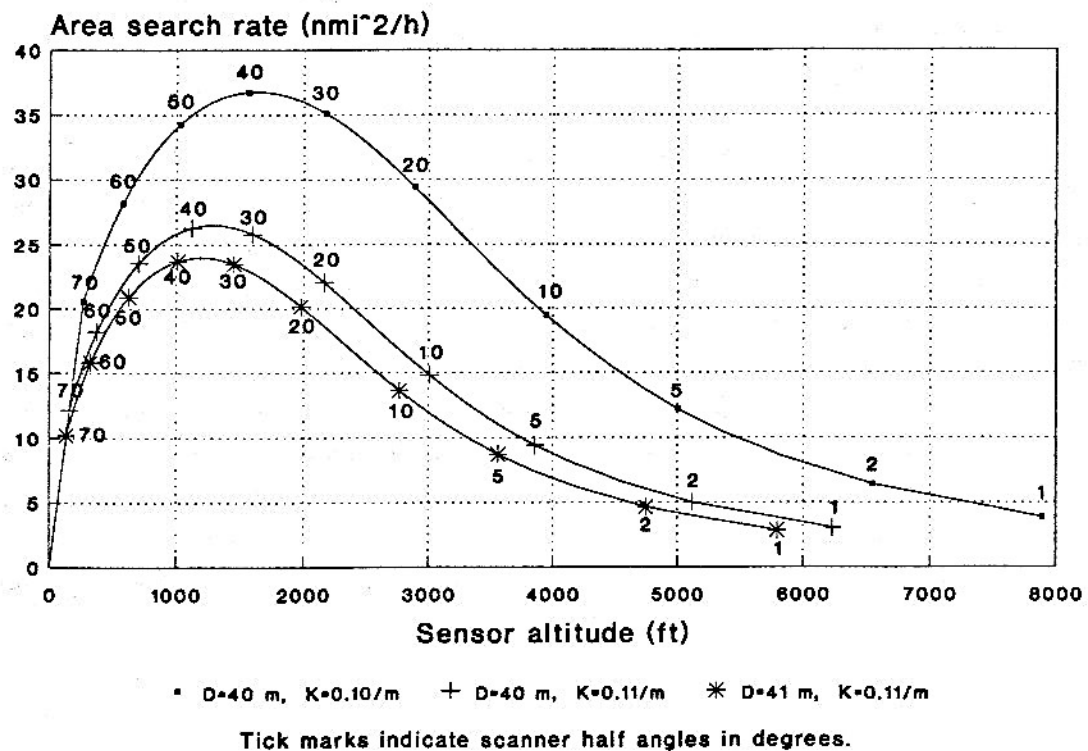

Figure 40. Comparison of calculated nighttime area search rates for baseline ASW lidar for combinations of submarine deck depth and seawater attenuation coefficient.

63

The upper two curves of figure 40 show that for D = 40 m, the maximum search rate decreases to 26.5 nmi^2/h from 36.8 nmi^2/h (a 28% reduction) if K increases from 0.10/m to 0.11/m (only a 10% increase). Thus, maximum search rate is very sensitive to the value of K. (Note: It should be possible to design the lidar to measure and display K continuously during USW operations to permit optimum performance under varying conditions.)

The lower two curves of figure 40 illustrate the effect of assumed target deck depth on search rate. For the given set of conditions, if the assumed depth increases to 41 m from 40 m (only a 2.5% increase), the maximum search rate decreases to 24.0 nmi^2/h from 26.5 nmi^2/h (a 9% decrease). That is, maximum search rate is even more sensitive to variations in assumed target depth than in attenuation coefficient. Operationally, if there are uncertainties in target depth, one may have to operate the sensor aircraft at a lower than optimum altitude to insure sanitization of an area.

Effect of Sensor Aircraft Speed on Search Rate

One of the approaches to increasing search rate is to fly faster. For non-geometry-limited situations, as search rate is increased there is a corresponding decrease in detection depth capability; the amount of decrease depends upon which method is used to achieve the increased search rate. Although flying significantly faster may not often be a viable option, it does represent the approach to increased search rate that results in the least degradation in detection depth capability.

Figure 41 shows the effect of doubling and tripling sensor aircraft speed to 170 and 255 kn from the baseline value of 85 kn. The other baseline conditions given in Table 1 are unchanged except for the attenuation coefficient, which was assumed to be 0.07/m, the target depth, which was kept constant at 40 m, and the sensor aircraft altitude, which was treated as a variable. For the geometry-limited straight-line portions of the curves, the search rates are exactly two and three times as large for the 170- and 255-kn speeds as for 85 kn. However, for altitudes above about 750 ft, the sensitivity-limited condition sets in. Thus the maximum search rate at the highest speed is 202.7 nmi^2/h and is 94.5 nmi^2/h for the lowest speed; that is, a 2.1-fold increase in maximum search rate results from flying three times as fast. The increase is less than threefold because it is necessary to reduce the lateral field of view of the scanner by a larger amount at the higher speed to maintain the detection depth capability at 40 m.
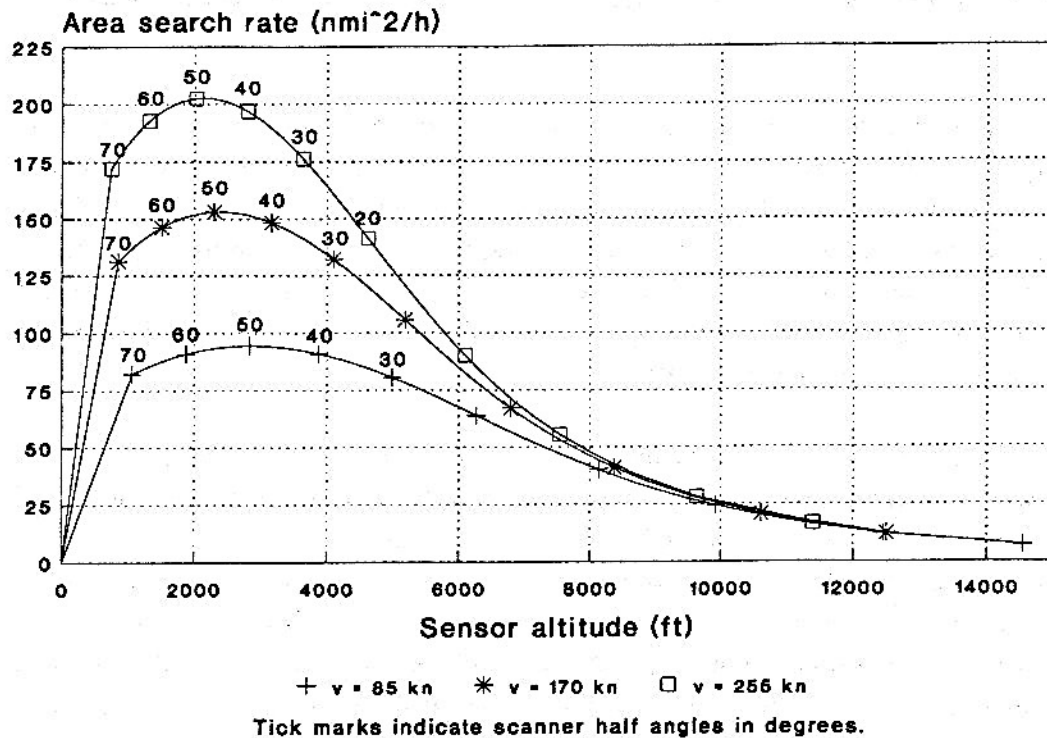
Area search rate (nmi^2/h)

Sensor altitude (ft)

+ v = 85 kn   * v = 170 kn   □ v = 255 kn

Tick marks indicate scanner half angles in degrees.

Figure 41. Effect of sensor aircraft speed on baseline ASW lidar nighttime area search rate for 40-m submarine deck depth and K = 0.07/m.

See text for assumptions.

Effects of Beam Diameter on Lidar Performance

The diameter of the laser beam as it enters the water can have a significant effect on the performance of a USW lidar because of several factors. First, if the beam diameter is large at the surface, it will be even larger at the target location, such that the target will intercept and return only a small fraction of the radiant energy of the pulse; that is, the geometric form factor F will have a low value. Second, if the beam diameter is large and the laser light strikes the sea surface and a (large) target obliquely, the pulse will be smeared out in time; that is, the received pulse duration t_r will be increased, by perhaps an order of magnitude. Furthermore, an increase in t_r will reduce the contrast between the target and the water by causing an increase in the reflectance ρ_w of the adjacent slab of water by increasing its effective thickness. An inspection of equations (14) and (15) shows that increases in t_r and ρ_w and a decrease in F cause their left sides to increase; to maintain constant

65

performance, the right sides of those equations must be increased correspondingly, perhaps by increasing the laser average power P_{av}. Thus it appears desirable to maintain the beam diameter as small as possible consistent with other parameters of the system such as maximum laser pulse repetition rate.

As stated earlier, the model can accommodate three approaches to beam diameter management: (1) constant beam divergence solid angle, (2) constant beam diameter at the sea surface, or (3) constant laser spot area at the sea surface. It was also stated that for a circular scanner, all three conditions occur simultaneously. Because there are certain advantages to be gained by use of other scanning methods, in which the angle of incidence and the slant range to the surface vary continuously during the scan cycle, it is appropriate to investigate the effects of beam diameter on performance.

For most of the illustrative examples given in this report, a constant beam diameter of 10 m was assumed for large targets (submarines) and 1 m for small targets (mines). It is instructive to examine the effects of beam diameter on detection depth capability and on possible tradeoffs with average power required to achieve a given level of performance. In figure 42 are plotted curves of demand index of performance for five values of beam diameter for the baseline conditions of Table 1 and horizontal lines of available index of performance corresponding to three values of average laser power. It is seen that as one reduces the beam diameter, the depth at which one can detect the target increases. For example, for an average power of 5 W, the detection depth increases to 55 m from 38 m as the beam diameter is decreased to 10 m from 40 m. Indeed, figure 42 shows that somewhat better performance (55-m detection depth) can be achieved with a 5-W lidar producing a 10-m beam than a 50-W lidar producing a 40-m beam (52-m detection depth). Of course, the lidar must be capable of operating at the higher PRFs needed when the smaller beam diameters are used.
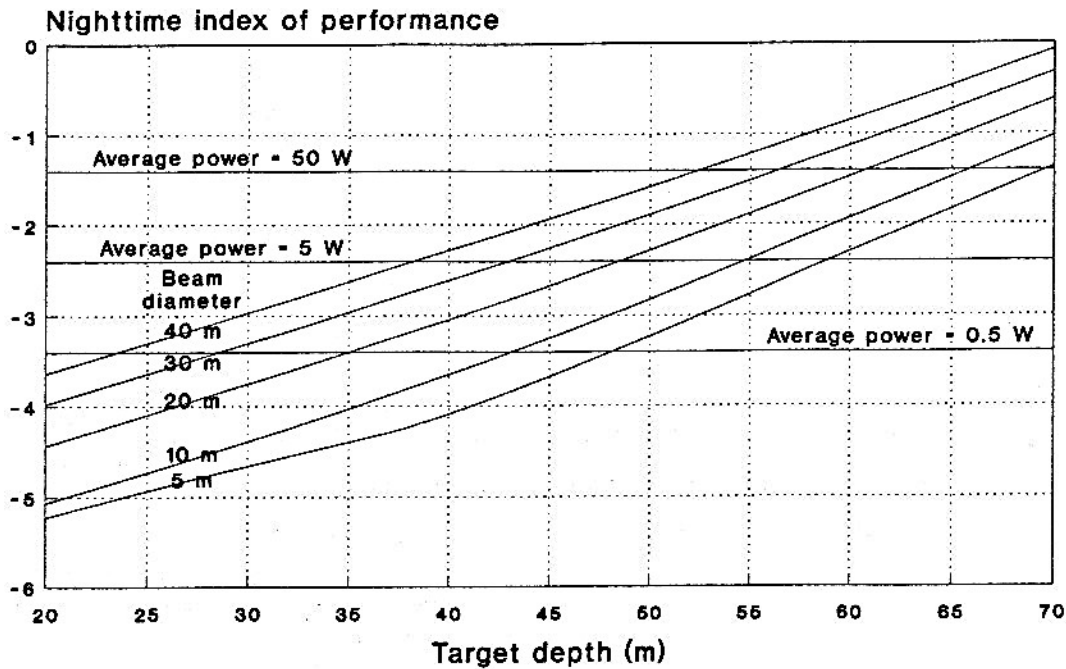
66

Figure 42. Index of performance required as a function of depth compared
to available performance index for five values of beam diameter
at the sea surface and three values of average power.

It is assumed that 21st century line-scanning USW lidars will be programmed to
adjust their beam divergence angles, scan angular velocities, and pulse repetition rates to
provide uniform detection depth capability over their entire swath widths. However, current
technology appears to be limited to lidars providing beams of divergence angles that remain
constant throughout the scan cycle. Figure 43 illustrates the difference in the rate of
detection depth dropoff with lateral scan angle for three beam management protocols:
(1) laser spot of constant area on the sea surface, (2) laser beam of constant diameter at the
sea surface, and (3) laser beam of constant solid divergence angle. It is seen that the dropoff
with increasing lateral scan angle is most severe for the (simplest) case of constant
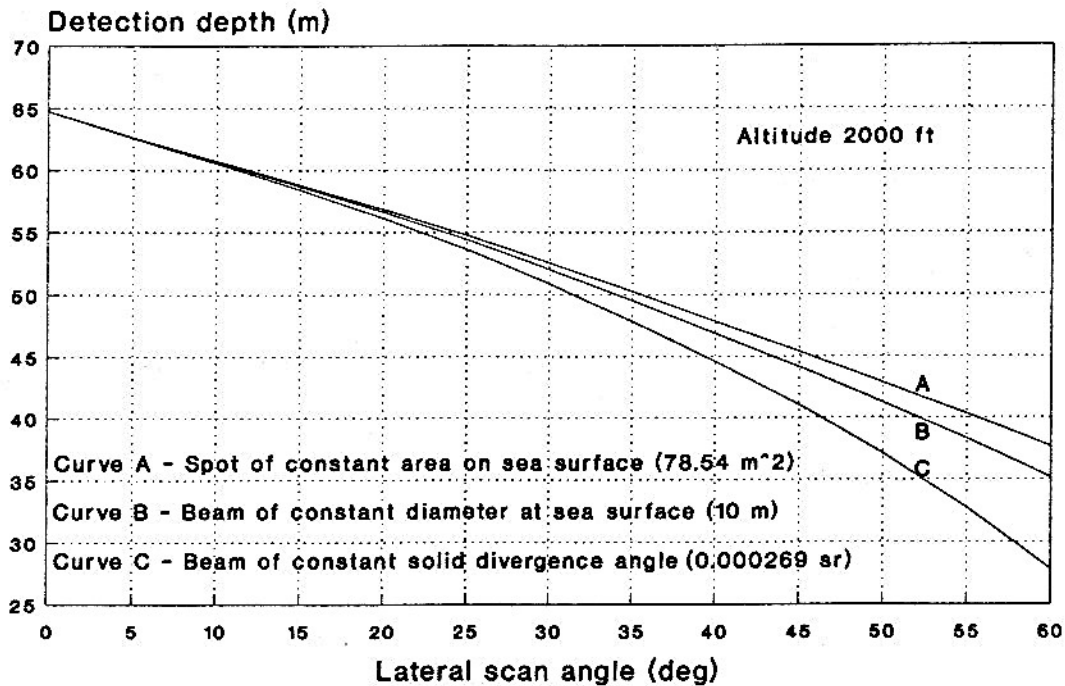divergence angle.

Detection depth (m)

Figure 43. Variation in detection depth capability as a function of lateral
scan angle for three beam management protocols.

Discussion

The foregoing results of exercising the lidar model were presented to illustrate, in a
number of specific examples, the capabilities of the model for exploring the design-
performance tradeoffs that are potentially available in current and future USW lidars. In
examining these results, the reader is cautioned not to draw generalized conclusions beyond
the assumptions that went into the computations. To address other conditions, the model
should be exercised anew.

68

VALIDATION AND ADJUSTMENT OF THE MODEL

During its development, the model was subjected to a number of "sanity" checks by comparing its "predictions" to data obtained from the NAWCADWAR OWL (Ocean Water Lidar) system. Reasonable agreement was obtained between the two in terms of detection depth although the model tended to yield somewhat greater values. It should be noted, however, that the model calculates detection depth capability whereas the OWL data represent detection depth achieved. In a programmed exercise it is generally not feasible to measure maximum detection depth. Thus, achieved depths would be expected to be less than achievable depths.

The model includes the parameter "SNR" whose value can be adjusted to correspond to various values of probability of detection and probability of false alarm. In some of the illustrative examples presented in this report, a value of SNR = 17 was assumed for $P_D = 0.95$ and $P_{FA} = 10^{-4}$. This P_{FA} value is rather high. Some lidar experts use a value of 17 dB for the required SNR, which is equivalent to SNR = 50; this value was also used in some of the calculations. If further comparisons of model predictions with real-world data so warrant, the assumed required value of SNR could be adjusted accordingly.

ACKNOWLEDGEMENT

REFERENCES

(a) A. K. Witt, J. G. Shannon, M. B. Rankin, and L. A. Fuchs III, *Air/Underwater Laser Radar, Test Results, Analysis, and Performance Predictions (U), ORIC (ORAD) Program (U)*, Naval Air Development Center (C) Report No. NADC-76005-20, January 1976.

(b) *RCA Electro-Optics Handbook*, Technical Series EOH-11 (1974).

(c) N. G. Jerlov, *Marine Optics*, Elsevier Oceanography Series, 14, Elsevier Publishing Company (1976).

(d) W. L. Wolfe and G. J. Zissis, editors, *The Infrared Handbook*, Environmental Research Institute of Michigan, 1978 (Rev. 1985).

(e) S. Fujimura, Pacific-Sierra Research Corporation, Private communication, 4 August 1993.

(f) D. E. Snead, *Area to Solid Angle Mapping Through the Air-Water Interface*, Pacific-Sierra Research Corporation, PSR Note 717, April 1986.

(g) S. H. Brewer, G. C. Davis, S. F. Fujimura, R. F. Lutomirski, and C. J. Swigert, *Airborne Imaging Scanner Technology Study*, Pacific-Sierra Research Corporation, PSR Report 1898, November 1989.

(h) U. S. Navy Marine Climatic Atlas of the World, Volume III, Indian Ocean, (NAVAIR 50-1C-530), (Rev. 1976).